Analysis of Cassini magnetic field observations over the poles of Rhea

Sven Simon,[1] Hendrik Kriegel,[2] Joachim Saur,[1] Alexandre Wennmacher,[1]
Fritz M. Neubauer,[1] Elias Roussos,[3] Uwe Motschmann,[2,4] and Michele K. Dougherty[5]

Received 21 March 2012; revised 4 May 2012; accepted 31 May 2012; published 18 July 2012.

[1] We analyze Cassini magnetic field observations from the only two polar flybys of Saturn's largest icy satellite Rhea (R2 on 02 March 2010 and R3 on 11 January 2011) which are scheduled between Saturn Orbit Insertion and the end of the mission in 2017. For the interpretation of these data, we apply estimations from simple analytical models as well as results from numerical hybrid simulations (kinetic ions, fluid electrons) of Rhea's interaction with the incident magnetospheric plasma. In-situ observations of exospheric neutral gas and pick-up ions suggest Rhea to be embedded in a tenuous gas envelope. However, the interaction of this gas with the magnetospheric flow does not make any measurable contributions to the magnetic field perturbations detected above the poles of the moon. Instead, the field perturbations observed in these regions mainly arise from the absorption of magnetospheric particles with large field-aligned velocities, impinging on the north and south polar surface of Rhea. In addition to numerous interaction features known from preceding Cassini flybys of Saturn's plasma-absorbing moons, the magnetic field data acquired above Rhea's poles reveal perturbations of the flow-aligned field component, corresponding to a draping/Alfvén wing pattern. Based on our hybrid simulations, we suggest that these signatures arise from the finite extension of Rhea's wakeside plasma void along the corotational flow direction, yielding a density gradient in corotation direction, and thereby generating a diamagnetic current from the Saturn-facing into the Saturn-averted hemisphere of the moon. This transverse current is responsible for generating a weak Alfvén wing pattern at Rhea which has been detected by the Cassini spacecraft during the R2 and R3 flybys. Due to the large gyroradii of the incident magnetospheric ions, this structure features a pronounced asymmetry with respect to the direction of the convective electric field. Results of our simulation, considering only plasma absorption on the moon, are in good agreement with Cassini magnetometer data from both flybys. At Saturn's icy satellites Tethys and Dione, the low value of the magnetospheric plasma beta most likely prevents the formation of similar currents and measurable flow-aligned magnetic field distortions.

Citation: Simon, S., H. Kriegel, J. Saur, A. Wennmacher, F. M. Neubauer, E. Roussos, U. Motschmann, and M. K. Dougherty (2012), Analysis of Cassini magnetic field observations over the poles of Rhea, *J. Geophys. Res.*, *117*, A07211, doi:10.1029/2012JA017747.

[1]Institute of Geophysics and Meteorology, University of Cologne, Cologne, Germany.
[2]Institute for Theoretical Physics, TU Braunschweig, Braunschweig, Germany.
[3]Max Planck Institute for Solar System Research, Katlenburg-Lindau, Germany.
[4]Institute for Planetary Research, German Aerospace Center, Berlin, Germany.
[5]Space and Atmospheric Physics Group, Blackett Laboratory, Imperial College, London, UK.

Corresponding author: S. Simon, Institute of Geophysics and Meteorology, University of Cologne, Zuelpicher Str. 49a, D-50674 Cologne, Germany. (simon@geo.uni-koeln.de)

0148-0227/12/2012JA017747

1. Introduction

[2] Since its arrival at Saturn in 2004, the Cassini spacecraft has paid numerous visits to the giant planet's multifaceted family of icy satellites. At the time of this writing, more than 160 orbits around the planet had already been accomplished by Cassini. During these orbits, the spacecraft has made 20 close flybys of Enceladus. This small icy moon was identified as the major source of magnetospheric plasma and neutral particles during the first year of Cassini's tour in the Saturnian system [e.g., *Dougherty et al.*, 2006]. In addition, the spacecraft has paid visits to several of the other icy satellites in the inner and middle magnetosphere: Dione –which was recently found to possess a tenuous, sputtering-induced exosphere

[*Simon et al.*, 2011a; *Tokar et al.*, 2012]–, Tethys, and Saturn's largest icy satellite Rhea.

[3] Rhea (radius R_{rh} = 764 km) orbits its parent planet on an equatorial and circular orbit at an L shell value of 8.74. Despite a number of highly puzzling observations during the first Rhea flybys –such as the identification of a ring system around the moon in energetic electron data [*Jones et al.*, 2008] which was not confirmed by optical observations [*Tiscareno et al.*, 2010]–, only four targeted Rhea encounters have been scheduled during Cassini's mission. Three of these encounters (termed R1, R2 and R3) have already taken place at the time of this writing.

[4] During the first close Rhea flyby (R1 on 26 November 2005), Cassini passed through the plasma wake downstream of the moon at a distance of about 0.7 R_{rh}. Observations made by the Cassini magnetometer (MAG) [*Dougherty et al.*, 2004] during this encounter suggested Rhea to be an electromagnetically inert object that interacts with the impinging magnetospheric plasma mainly by absorbing the particles incident upon its surface. Subsequently, Cassini accomplished two polar flybys of Rhea in 2010 and 2011 (R2 on 02 March 2010 at 23.3 Saturnian Local Time and R3 on 11 January 2011 at 13.3 Saturnian Local Time). When passing above Rhea's north pole during R2, Cassini's Ion and Neutral Mass Spectrometer (INMS) detected the presence of a tenuous exosphere around the moon [*Teolis et al.*, 2010]. This exosphere, consisting mainly of molecular oxygen and a minor contribution of carbon dioxide, was found to be sustained by chemical decomposition of the surface water ice due to sputtering by Saturn's magnetospheric plasma. The detection of a dilute, sputtering-induced atmosphere around Rhea is consistent with the predictions of *Saur and Strobel* [2005] who had explored the possible existence of atmospheres around Saturn's icy satellites before the first Cassini flybys took place. The question of whether the existence of this atmosphere is confirmed by INMS observations from the subsequent, south-polar R3 encounter has so far not been addressed in the peer-reviewed literature.

[5] During both polar flybys, the Cassini MAG instrument detected significant magnetic field perturbations inside the Rhea flux tube, the surface of which is defined by the bundle of field lines tangential to the solid body of the moon. While *Santolík et al.* [2011] applied Cassini particle and magnetic field observations to demonstrate the presence of intense plasma wave emissions at the time of the R2 encounter, the origin of the large-scale magnetic field perturbations seen during R2 and R3 has so far not been addressed in the literature. Especially, MAG data from both flybys contain strong perturbations of the flow-aligned magnetic field component ("draping"). At first glance, this seems untypical for the plasma interaction of an obstacle that affects the incident magnetospheric plasma mainly by absorbing it [see, e.g., *Khurana et al.*, 2008; *Roussos et al.*, 2008a; *Simon et al.*, 2009].

[6] In this paper, we present a detailed analysis of the Cassini magnetic field observations acquired during the two polar Rhea flybys R2 and R3. The origin of the observed field perturbations is discussed, on the one hand, by applying simple analytical models of the interaction between an inert moon and the incident flow. On the other hand, we continue the work of *Roussos et al.* [2008a] and present new hybrid (kinetic ions, fluid electrons) simulations of Rhea's interaction with the magnetospheric plasma, taking into account the upstream flow conditions observed during R2 and R3.

[7] This paper is organized as follows: in section 2, we classify the interaction between Rhea and the incident magnetospheric flow. After providing a brief overview of the ambient magnetospheric plasma parameters at Rhea's L shell (section 2.1), we derive an upper limit for the contribution of Rhea's exosphere to the observed magnetic field perturbations (section 2.2). In section 3, we focus on the interpretation of MAG data from R2 and R3. A brief discussion of the two flyby trajectories (section 3.1) is followed by an analysis of MAG data from the south polar R3 flyby in section 3.2 and results from complementary hybrid simulation runs in section 3.3. Our analysis of MAG data from the north-polar R2 encounter is provided in section 3.4. The paper concludes with a brief summary of our major findings (section 4).

[8] In the following sections, the spacecraft trajectories and the magnetic field components are always shown with respect to the Rhea Interaction System (RHIS). The (+x) axis of this Cartesian coordinate frame is aligned with the direction of ideal corotation, whereas the (+y) axis is directed from the center of Rhea toward Saturn. The (+z) axis completes the right-handed coordinate system, pointing northward, i.e. it is with good precision antiparallel to the ambient magnetospheric field $\underline{B}_0$ near Rhea's orbit. The origin of the RHIS coincides with the center of Rhea. The unit vectors of the RHIS will be referred to as $\{\underline{e}_x, \underline{e}_y, \underline{e}_z\}$.

2. Key Parameters of Rhea's Magnetospheric Interaction

[9] This section focuses on the incident magnetospheric flow conditions near Rhea's orbit. Besides, we assess a possible influence of Rhea's dilute exosphere on the moon's magnetic environment.

2.1. Upstream Flow Conditions

[10] Near Rhea's orbit, the magnetospheric plasma mainly consists of water group ions (mass m_i = 17 amu) with a number density of about n_0 = 6 cm^{-3} and a temperature of kT_i = 200 eV [cf. *Khurana et al.*, 2008, Table 1; *Wilson et al.*, 2010, Table 2]. Measurements of thermal ion properties from the R1 encounter and a more distant, non-targeted flyby on 30 August 2007 (sometimes termed "R1.5") suggest the incident magnetospheric flow to subcorotate, with its bulk velocity u_0 relative to Rhea being about 30% smaller than the full corotation speed of 57 km/s, hence u_0 = 40 km/s [*Wilson et al.*, 2010]. During R2 and R3, the background magnetic field possessed a magnitude of about B_0 = 21 nT (see also section 3), which is slightly smaller than observed during the initial R1 flyby in 2005 [see *Khurana et al.*, 2008, Figure 6]. The background field near Rhea's orbit points mainly in ($-z$) direction, i.e. it is with good precision antiparallel to Saturn's spin axis/magnetic moment. Based on data from the Cassini Plasmaspectrometer CAPS, *Sittler et al.* [2006, 2007] derived a temperature of kT_e = 10 eV for the thermal electrons at Rhea's L shell, i.e. more than an order of magnitude smaller than the value for the ions. The corresponding plasma betas are $\beta_e = \frac{2\mu_0 n_0 k T_e}{B_0^2}$ =

0.05 (electrons) and $\beta_i = \frac{2\mu_0 n_0 k T_i}{B_0^2} = 20\ \beta_e = 1.10$ (ions), respectively. A possible contribution of the hot magnetospheric plasma component to the total pressure [*Sergis et al.*, 2010] is not taken into account here.

[11] Thus, Rhea is exposed to a sub-Alfvénic, subsonic and sub-magnetosonic magnetospheric plasma flow (Alfvénic Mach number $M_A = 0.9$, sonic Mach number $M_S = 0.8$, magnetosonic Mach number $M_{MS} = 0.6$), i.e. the incident flow conditions are qualitatively similar to those at the other large icy satellites Enceladus [*Saur et al.*, 2008; *Kriegel et al.*, 2009], Tethys [*Simon et al.*, 2009] and Dione [*Simon et al.*, 2011a].

[12] However, it should also be noted that Rhea's magnetospheric environment features a rather high level of variability. For instance, the magnitude of the background magnetospheric field observed during R1 was about 3 nT larger than during R2 and R3 [*Khurana et al.*, 2008]. The ambient plasma density observed during individual flybys may also differ from the above value by up to 30% (E. Roussos et al., Energetic electron observations of Rhea's magnetospheric interaction, submitted to *Icarus*, 2012). Due to this variability, Rhea may occasionally be exposed to a super-alfvénic plasma flow [*Roussos et al.*, 2008a], similar to the upstream situation at Titan [*Neubauer et al.*, 1984].

[13] A peculiar feature of Rhea's magnetospheric interaction stems from the large gyroradii of the magnetospheric upstream ions: the parameters provided above yield a value of $r_g = m_i v_{th}/(eB_0) = 491$ km for the gyroradius ($v_{th} = \sqrt{3kT_i/m_i} = 58$ km/s $= 1.45\ u_0$: thermal ion velocity), i.e. about 64% of the radius of Rhea. Therefore, the absorption of magnetospheric particles at the moon's surface is expected to possess a pronounced asymmetry with respect to the direction of the convective electric field. At Enceladus ($r_g = 10.8$ km $= 0.04\ R_E$), Tethys ($r_g = 30.9$ km $= 0.06\ R_T$) and Dione ($r_g = 92.3$ km $= 0.16\ R_D$), asymmetries due to finite gyroradius effects are expected to play a far less important role (where R_j, $j = E, T, D$, denotes the respective satellite radius, values of r_g derived from Table 1 in *Khurana et al.* [2008]).

2.2. Magnetic Visibility of Rhea's Exosphere

[14] Based on data from Cassini's Ion and Neutral Mass Spectrometer (INMS) collected during R2, *Teolis et al.* [2010] recently identified a tenuous, sputtering-induced atmosphere around Rhea, consisting mainly of molecular oxygen and a minor contribution of carbon dioxide. Simultaneously, the Cassini Plasmaspectrometer (CAPS) observed outflowing positive and negative pick-up ions. However, *Khurana et al.* [2008] as well as *Roussos et al.* [2008a] succeeded in explaining MAG data from the first close Rhea encounter (R1) by considering Rhea an electromagnetically inert object that does not possess an atmosphere.

[15] One reason for this apparent discrepancy is that the trajectory of the R1 encounter was not suitable for identifying signatures of a possible gas envelope around Rhea in the magnetic field data. During R1, Cassini passed through Rhea's plasma wake, with the spacecraft trajectory being confined to the ($z = 0$) plane. If a flyby above or below Rhea's equatorial plane had been available, the orientation of the measured B_y perturbations could have been employed to clearly discriminate between a mainly plasma-absorbing obstacle and an interaction scenario that is dominated by mass/momentum loading (see Figure 10 in *Khurana et al.* [2008] and Figure 1 in *Simon et al.* [2009]). However, for a flyby like R1 that occurred in Rhea's orbital plane, the B_y perturbation is almost zero in both cases (assuming that a possible atmosphere does not possess a pronounced north-south asymmetry).

[16] Thus, if Rhea's atmosphere caused any measurable magnetic field perturbations, the polar flybys R2 and R3 would have been suitable to identify such signatures. However, based on the parameters provided by *Teolis et al.* [2010], we expect the gas envelope around Rhea to be magnetically invisible even during these close encounters. To decide whether Rhea's exosphere/ionosphere could generate any noticeable magnetic field perturbations, one has to compare the Alfvén conductance Σ_A of the ambient magnetospheric plasma,

$$\Sigma_A = \frac{1}{\mu_0 v_A \sqrt{1 + M_A^2}} \qquad \text{for} \qquad \underline{u}_0 \perp \underline{B}_0 \tag{1}$$

(where $v_A \equiv |\underline{v}_A| \equiv \left|\frac{B_0}{\sqrt{\mu_0 n_0 m_i}}\right|$: Alfvén velocity), against the Pedersen conductance of the moon's ionosphere. These two quantities define the *interaction strength parameter*

$$\overline{\alpha} \equiv \frac{\Sigma_P}{\Sigma_P + 2\Sigma_A} \qquad (0 \le \overline{\alpha} \le 1), \tag{2}$$

where Σ_P denotes the Pedersen conductance [*Saur et al.*, 1999; *Saur and Strobel*, 2005].

[17] If $\overline{\alpha} = 0$, the atmosphere does not make any contribution at all to the plasma interaction, while in the other extreme case of $\overline{\alpha} = 1$, the magnetic field perturbations caused by the presence of the atmosphere reach their maximum possible value and the plasma flow within the wing tubes is decelerated to complete stagnation.

[18] Based on the upstream flow parameters provided in section 2.1, we obtain a value of $\Sigma_A = 13.2$ S for the Alfvén conductance in the Rhea scenario. An order-of-magnitude estimate for the Pedersen conductance Σ_P can be obtained from the atmospheric parameters of *Teolis et al.* [2010] who derived a total atmospheric O_2 content of $N_{tot} = 2.5 \cdot 10^{29}$ molecules. For our estimate, we assume the spatial distribution of the neutral gas around Rhea to be spherically symmetric and to be prescribed by equation 1 in the work of *Saur and Strobel* [2005], i.e.

$$n_n(r) = n_{n,0} \left(\frac{R_{rh}}{r}\right)^2 \exp\left(\frac{R_{rh} - r}{D}\right), \tag{3}$$

where r denotes the distance to the center of Rhea. From the work of *Saur and Strobel* [2005], we adopt a value of $D = 100$ km for the depletion length scale, while the base density n_0 can be derived from the total gas content of the atmosphere N_{tot} according to

$$n_{n,0} = \frac{N_{tot}}{4\pi R_{rh}^2 D}. \tag{4}$$

[19] From the work of *Simon et al.* [2011a], we adopt a value of $\kappa = 1 \cdot 10^{-8}$ cm^3/s for the reaction rate between

magnetospheric water group ions and oxygen molecules at a relative velocity of u_0 = 40 km/s, considering charge-exchange reactions and elastic collisions. This allows to compute the (effective) ion-neutral collision frequency according to $\nu(r) = \kappa n_n(r)$. The ratio of the ion gyrofrequency $\Omega_i = \frac{eB_0}{m_i}$ and the collision frequency is then applied to compute the local Pedersen conductivity according to

$$\sigma_P(r) = \frac{en_0}{B_0} \cdot \frac{\frac{\Omega_i}{\nu(r)}}{\left(\frac{\Omega_i}{\nu(r)}\right)^2 + 1}, \quad (5)$$

see equation (27) in the work of *Saur et al.* [1999].

[20] By numerically integrating equation (5), we now compute the Pedersen conductance Σ_P along a magnetic field line that intersects Rhea at the north pole, i.e.

$$\Sigma_{P,1} = \int_{r=R_{rh}}^{\infty} \sigma_P(r)\mathrm{d}r, \quad (6)$$

and along a magnetic field line that is tangential to the solid body of the moon:

$$\Sigma_{P,2} = \int_{z=0}^{\infty} \sigma_P\left(\sqrt{z^2 + R_{rh}^2}\right)\mathrm{d}z. \quad (7)$$

[21] These two values constitute a lower ($\Sigma_{P,1}$) and an upper ($\Sigma_{P,2}$) limit for the Pedersen conductance in the Rhea scenario; see Figure 6 in the work of *Neubauer* [1998] for illustration. The estimated values of the Pedersen conductance range between $\Sigma_{P,1}$ = 0.11 S and $\Sigma_{P,2}$ = 0.43 S, respectively, corresponding to an interaction strength of $4.2 \cdot 10^{-3} \leq \overline{\alpha} \leq 1.6 \cdot 10^{-2}$. Thus, the contribution of Rhea's atmosphere to the magnetic field signatures arising from the moon's interaction with the upstream flow can be considered negligible. The pick-up ions generated at Rhea can be treated as test particles that are inserted in a predefined electromagnetic field configuration. For comparison, the parameters provided by *Saur et al.* [2007] suggest an interaction strength of $\overline{\alpha}$ = 0.6 for Enceladus' magnetospheric interaction. Besides, as will be shown in section 3, the key features of the magnetic field observations made during the R2 and R3 flybys can be explained by means of a numerical model that considers only the plasma-absorbing body of Rhea, but not its exosphere. Apart from the estimations provided above, the analysis of the magnetic field data therefore provides independent evidence that Rhea's exosphere was indeed "magnetically invisible" at the times of the R2 and R3 encounters.

[22] We would briefly like to note that Rhea's exosphere might exhibit some degree of time variability, similar to what *Simon et al.* [2011a] found at Dione due to the time-dependency of energetic particle fluxes in Saturn's radiation belts. If at certain time periods Rhea's energetic particle environment is similar to what Voyager 1 saw, then both the atmospheric particle content and the associated magnetic field perturbations will be significantly stronger [*Saur and Strobel*, 2005]. For the conditions of the Voyager 1 flyby, these authors derived an interaction strength of $\overline{\alpha}$ = 0.4. Voyager 1 estimates for the energetic particle influx to Saturn's icy satellites showed to be consistently much higher than what has been measured by Cassini [e.g., *Roussos et al.*, 2008b], thereby possibly generating an atmosphere around Rhea that was "magnetically visible" at that time.

3. Rhea Flybys R2 and R3

[23] In this section, we shall present the Cassini magnetic field observations from the two polar Rhea encounters. For the interpretation of the data, both analytical estimations and plasma simulations with the hybrid code AIKEF [*Müller et al.*, 2011] will be applied.

3.1. Flyby Trajectories

[24] Figure 1 displays the trajectories of the R2 and R3 encounters. As can be seen, Cassini passed above Rhea's north pole during R2, approaching the moon from the Saturn-averted side. Within the interval shown in the figure, the flyby trajectory was nearly parallel to the (z = 0) plane and only slightly inclined with respect to the y axis: in the inbound region of R2 (i.e. for $y < 0$), Cassini was located in the downstream half-space (i.e. at $x > 0$), whereas in the outbound segment ($y > 0$), the spacecraft traveled through the upstream half-space ($x < 0$). The subsequent R3 encounter occurred below Rhea's south pole and featured a strong similarity to the geometry of R2. Again, the spacecraft trajectory was nearly parallel to the (z = 0) plane and possessed only a small inclination against the y axis. However, during R3 Cassini was located downstream of Rhea ($x > 0$) in the Saturn-facing half-space ($y > 0$), whereas the segment of the flyby trajectory in the Saturn-averted half-space ($y < 0$) lead through the ($x < 0$) half-space. As can also be seen from Figure 1, closest approach of both flybys was located at a distance of about only 0.1 R_{rh} above the surface of Rhea.

[25] We would like to note that only one additional close flyby of Rhea is scheduled for the remaining five years of the Cassini mission: during the northbound R4 encounter on 09 March 2013, the spacecraft is anticipated to achieve a closest approach altitude of 1000 km (=1.3 R_{rh}), i.e. about an entire order of magnitude larger than during R2 and R3.

[26] In the following sections, we shall discuss the observations made by the Cassini magnetometer during R2 and R3, as displayed in Figure 2. We will commence our discussion with the R3 flyby, since the data acquired during this passage allow for a much easier depiction of the key features of the interaction than the R2 data set.

3.2. Flyby R3: MAG Data

[27] The magnetic field signatures observed during R3 are displayed in Figure 2 (right). The vertical magenta lines indicate Cassini's passages through the surface of the Rhea flux tube $\sqrt{x^2 + y^2} = R_{rh}$. Although the R3 trajectory was located below the south pole and did not intersect the moon's geometric plasma shadow, the magnetic field observations reveal several features immediately indicative of a plasma-absorbing obstacle. The B_z component exhibits a compression signature inside the Rhea flux tube, i.e. $|B_z|$ is enhanced. Similar enhancements of $|B_z|$ have also been observed in the plasma wakes of Tethys and Dione as well as during the R1 flyby of Rhea [*Khurana et al.*, 2008; *Roussos et al.*, 2008a; *Simon et al.*, 2009, 2011a]. Such signatures arise from a void in the magnetospheric plasma density due to the absorption of the incident flow at the moon's surface.

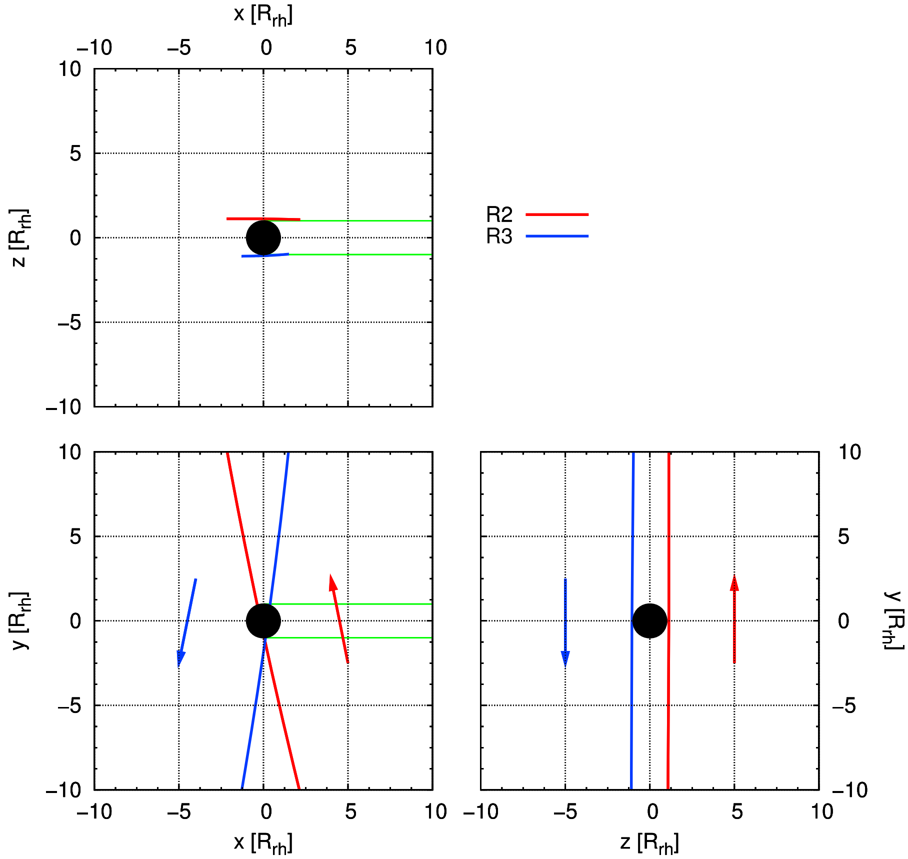

Figure 1. Cassini's trajectories during Rhea flybys R2 (red) and R3 (blue) in RHIS coordinates. Closest approach of both flybys occurred near $y = 0$. During R2, Cassini achieved its closest approach altitude of 0.13 R_{rh} on 02 March 2010 at 17:40:35. Closest approach of R3 occurred on 11 January 2011 (04:53:25) at an altitude of 0.09 R_{rh}. The green lines denote the outer boundaries of Rhea's geometric plasma shadow, i.e. the cylinder $\sqrt{y^2 + z^2} = R_{rh}$ for $x \geq R_{rh}$.

The resulting deficit of plasma pressure is then compensated by an enhanced magnetic pressure, i.e. the field lines are dragged into the density cavity [see, e.g., *Simon et al.*, 2009, Figure 1]. While for the interaction between the Terrestrial moon and the supersonic solar wind, such field compression signatures occur only in the downstream region [*Kallio*, 2005], they expand to above and below the poles, if the flow incident upon the obstacle is subsonic. In this case, the bulk speed of the plasma is exceeded by its thermal speed, i.e. a significant number of particles possess large field-aligned velocities. Therefore, particles which were initially located north or south of Rhea can be absorbed as well, yielding an expansion of the density depletion region to the polar regions of the moon.

[28] The compression signature seen in B_z possesses a magnitude of about 2 nT. This value can be compared to the maximum field compression expected for the void region of the central wake which is (almost) completely evacuated [see *Khurana et al.*, 2008, Figure 3]. Based on the pressure balance equation

$$n_0 k(T_i + T_e) + \frac{B_0^2}{2\mu_0} = \frac{(B_0 + \delta B)^2}{2\mu_0} \tag{8}$$

and the upstream parameters provided in section 2.1, we find that a peak field perturbation δB of

$$\frac{\delta B}{B_0} = \sqrt{\beta_i + \beta_e + 1} - 1 \approx 0.47, \tag{9}$$

i.e. $\delta B \approx 9.8$ nT, can be achieved in Rhea's central wake. Thus, the perturbation observed below the south pole is about a factor of 5 smaller. This finding is consistent with the idea of the plasma in the south polar region being only partially depleted: only particles that impinge on Rhea's northern hemisphere with large field-aligned velocities are "missing" there. It should also be noted that additional B_z perturbations of nearly the same magnitude as in the central wake were observed outside the Rhea flux tube near $y = -2.1$ R_{rh}, $y = +3.0$ R_{rh} and $y = +9.0$ R_{rh}. These signatures may possibly arise from fresh plasma injections in Saturn's equatorial plane, which may have occurred coincidentally [see, e.g., *Burch et al.*, 2007]. Similar events were found to "contaminate" the interaction signatures observed during a recent wakeside flyby of Dione [*Simon et al.*, 2011a].

[29] Equation (8) also illustrates why the magnitude of the B_z perturbations observed *over the poles* of Rhea (compared to the background field strength) is much larger than the compression signatures detected in the *wake* of Tethys

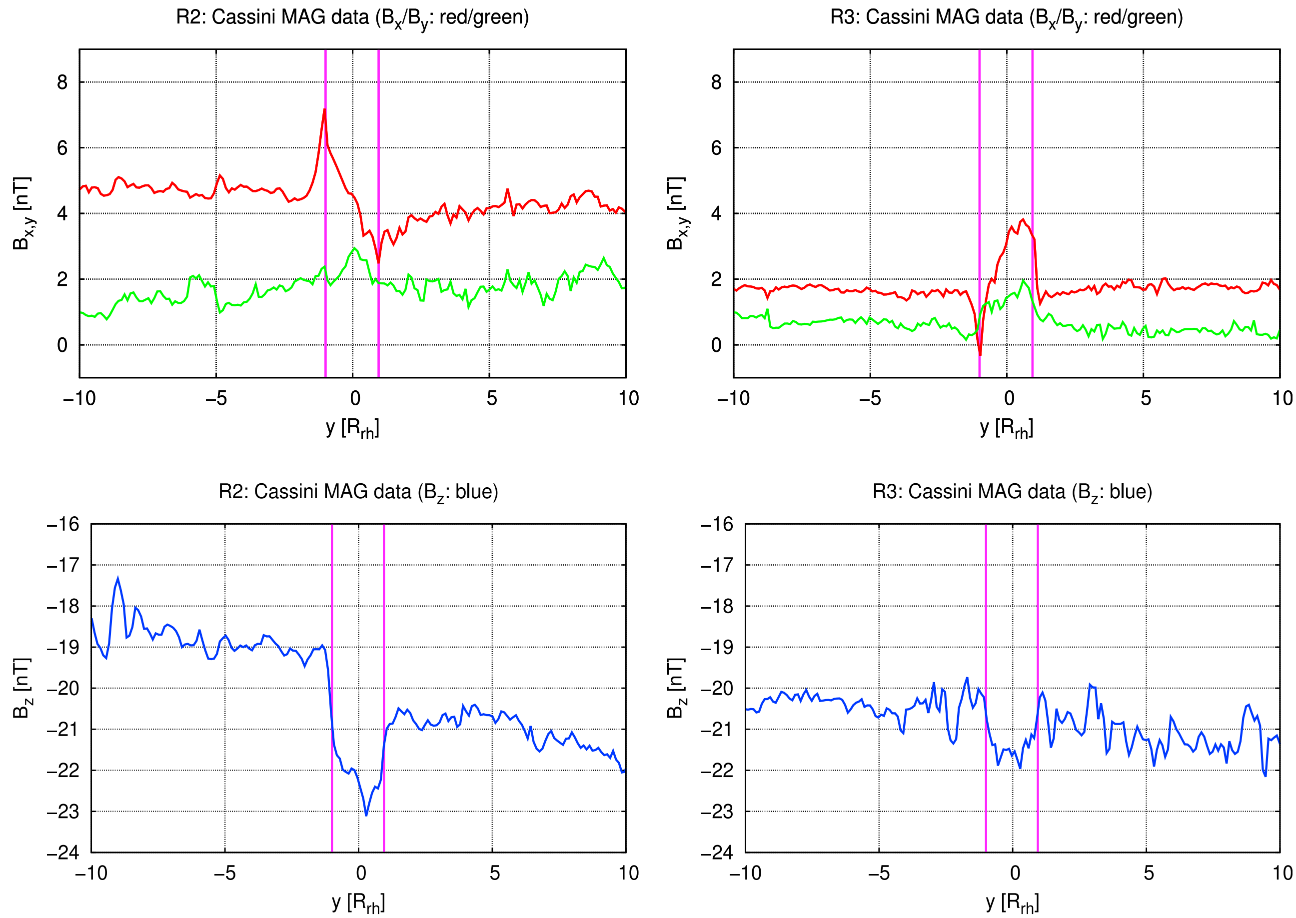

Figure 2. Cassini MAG observations during Rhea flybys (left) R2 and (right) R3 in RHIS coordinates. The magnetic field components are shown in red (B_x), green (B_y) and blue (B_z), respectively. The vertical magenta lines denote Cassini's passages through the surface of the Rhea flux tube $\sqrt{x^2 + y^2} = R_{rh}$. Despite the slight deviations of $\underline{B}_0$ from being aligned with the negative z axis, this expression provides a very good approximation for the surface of the flux tube.

during the only targeted flyby [*Khurana et al.*, 2008; *Simon et al.*, 2009]. The above expression can be rewritten as

$$\frac{B_0 + \delta B}{B_0} = \sqrt{1 + \beta_i + \beta_e}. \qquad (10)$$

[30] Hence, the relative magnitude of the maximum field perturbation is determined by the total plasma beta of the ambient magnetospheric flow. The more important the impact of flow dynamics, the larger are the compression signatures in the magnetic field. While at Rhea, the value of $\beta_i + \beta_e$ is of the order of one, the by far stronger magnetospheric field near Tethys' orbit (B_0 = 167 nT) yields a value of $\beta_i + \beta_e = 0.02$, thereby allowing for a peak field perturbation of only 1% of the background field [see also *Simon et al.*, 2009].

[31] The slight enhancement of B_y observed within the Rhea flux tube (see Figure 2) arises from the aforementioned field compression due to plasma absorption. In the ($z < 0$) half-space, the field compression yields a region of $B_y < 0$ for $y < 0$ and a region of $B_y > 0$ for $y > 0$ [see *Simon et al.*, 2009].

[32] As can be seen from the (x, y) projection in Figure 1, Cassini crossed regions of both ($y < 0$) and ($y > 0$) while being located inside the Rhea flux tube. Therefore, one would expect the spacecraft to pass through both the ($B_y > 0$) and the ($B_y < 0$) perturbation region. The fact that only the ($B_y > 0$) distortion was detected is consistent with CAPS observations from R1 and R1.5 [*Wilson et al.*, 2010], suggesting a slight tilt of the ambient bulk speed away from Saturn. Such a tilt would rotate the interaction signatures around the z axis in clockwise direction, thereby shifting the region of positive B_y further into the Rhea flux tube. The region of ($B_y < 0$) was then probably missed by Cassini due to the slight tilt of the trajectory. We will address this feature again when discussing our hybrid simulation results in section 3.3.

[33] It is very important to note that Cassini also observed a non-vanishing, positive B_x perturbation below Rhea's south pole, possessing nearly the same magnitude as the perturbation seen in B_z. In general, one would expect such a B_x distortion to arise from field line draping, i.e. from the formation of an Alfvén wing due to an interaction between the obstacle's ionosphere or intrinsic magnetic field and the incident plasma [*Neubauer*, 1980, 1998]. However, as inferred in section 2.2, Rhea's gas envelope is far too dilute to cause such strong perturbations of the magnetospheric

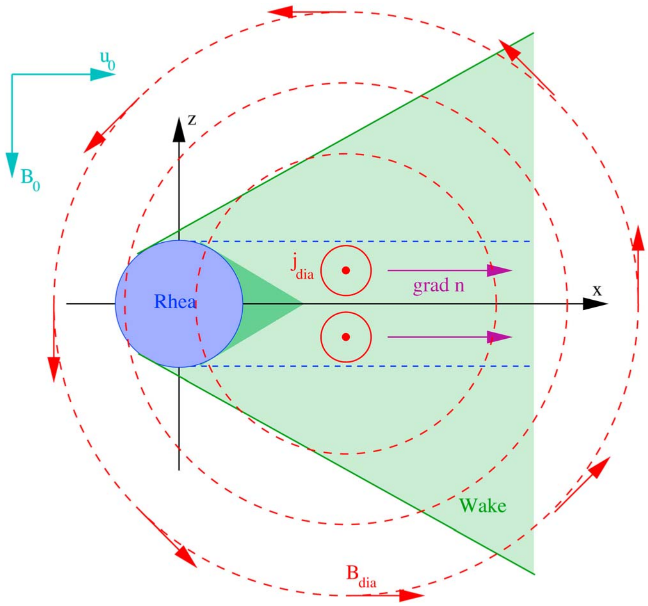

Figure 3. Diamagnetic currents arising from the finite length of Rhea's plasma wake along the corotational flow direction. For the (y = 0) plane of the RHIS (containing the background magnetic field $\underline{B}_0$ and the (co)rotational flow speed $\underline{u}_0$), the figure provides a schematic illustration of the magnetic field perturbations that arise from the refilling of Rhea's wake by magnetospheric particles with large field-aligned velocities. The void region of nearly zero plasma density is denoted in dark green, while the area shaded in light green depicts the rarefaction cone where the number density of the magnetospheric ions gradually increases with increasing distance to the moon in x direction. Within Rhea's geometric shadow (denoted by the cylinder $\sqrt{y^2+z^2} < R_{rh}$, dashed blue lines) the resulting density gradient along the positive x axis (magenta arrows) gives rise to a system of diamagnetic currents $\underline{j}_{dia}$, pointing out of the paper plane. By applying the right-hand rule to $\underline{j}_{dia}$, one verifies that above the north pole, the B_x component of the magnetic field generated by this current is negative, whereas below the south pole, it assumes a positive value. This field orientation is similar to what would be expected for the draping of the magnetic field around a conducting obstacle, as observed e.g. at Dione [*Simon et al.*, 2011a] and the plume of Enceladus [*Dougherty et al.*, 2005; *Kriegel et al.*, 2009]. The dashed circles and the arrows along them illustrate the magnetic field that would arise from $\underline{j}_{dia}$ alone. Outside Rhea's geometric shadow, the effect of the density gradient in (+x) direction is partially attenuated by the density gradient in ($-x$) direction along the outer flanks of the wake (boundaries of light green region), producing a diamagnetic current in (+y) direction. However, these perpendicular current systems do not fulfill $\nabla \cdot \underline{j}_\perp = 0$ by themselves. As revealed by our hybrid simulations, the diamagnetic currents in Rhea's wake are connected to the currents along the characteristics of an Alfvén wing.

field, and the moon was also found to be devoid of an internal magnetic field by *Khurana et al.* [2008]. Nonetheless, the observations shown here suggest that the interaction gives rise to a draping-like broad enhancement in B_x, being comparable to or even stronger than the distortions detected in the B_z and B_y components. As will be shown in the following, this B_x enhancement arises from the finite extension of Rhea's plasma wake along the corotational flow direction.

[34] In contrast to the Terrestrial moon –the wake of which is nearly devoid of plasma even at distances of several satellite radii [*Kallio*, 2005]–, the wake of a plasma-absorbing moon embedded in a submagnetosonic flow is refilled at rather short distances to the obstacle. As demonstrated by preceding hybrid simulations of Rhea's plasma interaction during the R1 flyby (for slightly different upstream parameters than provided in section 2.1, cf. *Roussos et al.* [2008a]), the number density of the plasma in Rhea's wake has already returned to 75% of the background value at a distance (in x direction) of only 1 R_{rh} to the surface of the obstacle. The resulting pressure gradient $\nabla p = \frac{\partial p}{\partial x}\underline{e}_x$ along the corotation direction gives rise to a diamagnetic current $\underline{j}_{dia}$ in ($-y$) direction,

$$\underline{j}_{dia} = \frac{\underline{B} \times \nabla p}{B^2} \approx \frac{\underline{B}_0 \times \nabla p}{B_0^2} = -\frac{1}{B_0}\frac{\partial p}{\partial x}\underline{e}_y, \quad (11)$$

where $\underline{B}$ in the first expression denotes the locally perturbed field in the interaction region. As a first approximation, we have assumed the magnetic field $\underline{B}$ in the expression for $\underline{j}_{dia}$ to be equal to the background magnetic field $\underline{B}_0$ outside the interaction region. As discussed above, a peak field strength of about 1.5 B_0 may locally be achieved in Rhea's central wake. In the central wake, this would yield an additional factor of 1/1.5 in equation (11). However, this deviation from the background field strength and the associated bending of the field lines toward the (y = 0) plane are neglected for the order-of-magnitude estimate of the diamagnetic current provided below. The diamagnetic current $\underline{j}_{dia}$ is thus parallel to the convective electric field $\underline{E}_0 = -\underline{u}_0 \times \underline{B}_0 = -u_0 B_0 \underline{e}_y$ of the undisturbed flow.

[35] The orientation of the density gradient as well as the current $\underline{j}_{dia}$ in the wake and the associated magnetic field perturbations are illustrated in Figure 3. This figure shows that below the south pole, the B_x perturbation arising from the diamagnetic current in Rhea's central wake is parallel to the positive x axis, whereas above the north pole, the associated B_x perturbation points in negative x direction. Thus, the diamagnetic current arising from the finite length of Rhea's wake produces field perturbations above the northern and southern poles that are qualitatively similar to what would be expected for field line draping around a conducting obstacle (cf. red dashed circles in Figure 3).

[36] To demonstrate that the proposed current $\underline{j}_{dia} \propto -\underline{e}_y$ can produce a sufficiently strong magnetic field below the south pole to explain the B_x enhancement observed during R3, let us assume that the thermal pressure $p(x)$ in the wake (note that the contributions of ram and magnetic pressure do not enter the pressure gradient term in the momentum equation of MHD and thus equation (11)) increases linearly from $p(x = 1\ R_{rh}) = 0$ at the surface of Rhea to $p(x = 4\ R_{rh}) = p_0 = n_0 k(T_i + T_e)$ at a distance of 3 R_{rh} to the surface. This estimate for the length of the wake is in good agreement with new hybrid modeling results for Rhea discussed in section 3.3. We also verified

from the simulations that the pressure gradient term and the Lorentz term indeed make up the dominant contributions in the momentum equation of the hybrid model within Rhea's wake.

[37] To obtain a simple analytical estimate for the magnetic field associated with the current j_{dia}, let us further assume that j_{dia} is constant within a cylinder of Radius 1 R_{rh} in y direction whose axis intersects the x axis at $x = 2.5\ R_{rh}$. The circular intersection area of this wire with the (x, z) plane covers a large fraction of the density depletion region downstream of Rhea [cf. *Roussos et al.*, 2008a]. The magnitude δB_{dia} of the magnetic field perturbation outside the current-carrying region is then given by

$$\delta B_{dia} = \frac{\mu_0 R_{rh}^2}{2\sqrt{(x-2.5R_{rh})^2+z^2}} \cdot \frac{p_0}{3B_0R_{rh}}. \quad (12)$$

This equation follows directly from Ampère's law by integrating along the circular magnetic field lines around the cylinder's axis (along which $|\delta \underline{B}_{dia}|$ is constant), yielding

$$\delta B_{dia} = \frac{\mu_0 j_{dia} \pi R_{rh}^2}{2\pi\sqrt{(x-2.5R_{rh})^2+z^2}}. \quad (13)$$

[38] In this expression, $\sqrt{(x-2.5R_{rh})^2+z^2}$ denotes the distance from the observer at point (x, y, z) to the axis of the cylinder and

$$j_{dia} = \frac{p_0}{3B_0R_{rh}} \quad (14)$$

is the diamagnetic current according to equation (11).

[39] Below the south pole ($x = 0$, $z = -1\ R_{rh}$), this yields a perturbation field of about $\delta B_{dia} \approx 0.75$ nT, which is of the same order of magnitude as the enhancement of B_x observed within the Rhea flux tube during R3. Hence, we suggest that the B_x perturbations observed below Rhea's south pole mainly arise from currents in the moon's intermediate wake. The question of how these diamagnetic currents are closed by field-aligned currents will be addressed in the discussion of our hybrid simulation results in section 3.3.

[40] However, we would like to point out that this estimation is only meant to demonstrate that a diamagnetic current arising from the finite length of Rhea's wake is able to produce a measurable B_x perturbation below the south pole that can in principle explain the observed increase of B_x. In reality, the geometry of the diamagnetic currents is far more complex than assumed here. Fully self-consistent hybrid simulations, as discussed in section 3.3, are required to determine the precise shape of the current systems in Rhea's wake and the field perturbations generated by them.

[41] The Rhea interaction scenario is particularly suitable for observing the magnetic field perturbations that arise from the finite length of the obstacle's wake. Although hybrid simulations suggest the extension of Tethys' plasma wake to be comparable to or even smaller than the length of Rhea's wake [*Simon et al.*, 2009], one would not expect to observe any strong perturbations of the flow-aligned field component at Tethys. As can be seen from equation (11), the magnitude of the diamagnetic current is inversely proportional to the magnetospheric field strength, which at Tethys is almost 8 times larger than at Rhea, yielding a plasma beta of only 0.02 [*Khurana et al.*, 2008; *Simon et al.*, 2009]. Thus, the current j_{dia} is not expected to make any measurable contributions to the magnetic field distortions at Tethys. One should therefore keep in mind that the extension of the wake is not the only controlling parameter for the magnitude of the diamagnetic current, but the magnetic field plays a key role as well.

[42] As demonstrated above, the finite extent of Rhea's wake along the corotation direction allows for a considerable flow-aligned field perturbation. However, as can also be seen from Figure 3, such a flow-aligned perturbation may occur only outside the ($z = 0$) plane. Within the ($z = 0$) plane, it leads to a field-aligned perturbation (i.e. $\delta \underline{B} \propto \underline{e}_z$) that strengthens the field upstream and decreases it downstream. The downstream decrease is probably obscured by the enhancement due to reduced plasma pressure. Upstream, the perturbation is without "competition" and should show an enhancement signature, as it would also be caused by mass/momentum loading [e.g., *Kriegel et al.*, 2009; *Simon et al.*, 2011a]).

[43] As can also be seen from Figure 3, the density gradient along the outer flanks of the interaction region (boundaries of the light green cone) possesses a component in *negative x* direction. Thus, it generates a diamagnetic current in positive y direction and a magnetic field that counteracts the effects of the finite wake extension along the corotation direction. In order for the B_x perturbation below the south pole to become positive (as observed during R3), the effect caused by the currents at the outer flanks of the wake must be overcompensated by the field arising from the density gradient in ($+x$) direction in the central wake. This is especially important in the polar regions where the wake flanks "touch" the solid body of the moon, cf. Figure 3. While outside Rhea's geometric shadow $\sqrt{y^2+z^2} < R_{rh}$ (and $x > 1\ R_{rh}$), density gradients in ($+x$) and ($-x$) direction occur, the density gradient inside the shadow region points exclusively in ($+x$) direction. The reason for this is that along the outer flanks of the density depletion region (light green cone), diamagnetic currents in ($+y$) direction are required to prevent the wake structure from collapsing, while inside the geometric shadow, the pressure gradient is stabilized by the shielding effect of Rhea's plasma-absorbing body. Thus, the currents in the shadow region (and the associated magnetic fields) do not experience an attenuation from nearby density gradients in ($-x$) direction and may even cause strong field perturbations above Rhea's poles. Numerical simulations (see section 3.3) are required to understand the magnetic field distortions caused by this complex system of wakeside currents.

[44] Finally, we would briefly like to note that the field perturbations seen in B_y and B_z are also caused by a diamagnetic current system, arising from the finite extension of the density cavity in y direction [*Colburn et al.*, 1967]. In the ($y > 0$) half-space, the pressure gradient points in ($+y$) direction, i.e. the resulting diamagnetic current is parallel to $\underline{e}_x$. In the ($y < 0$) half-space, the directions of both the density gradient and the resulting current are reversed. By applying the right-hand rule to these two current systems, one can easily verify that they are responsible for enhancing $|B_z|$ in

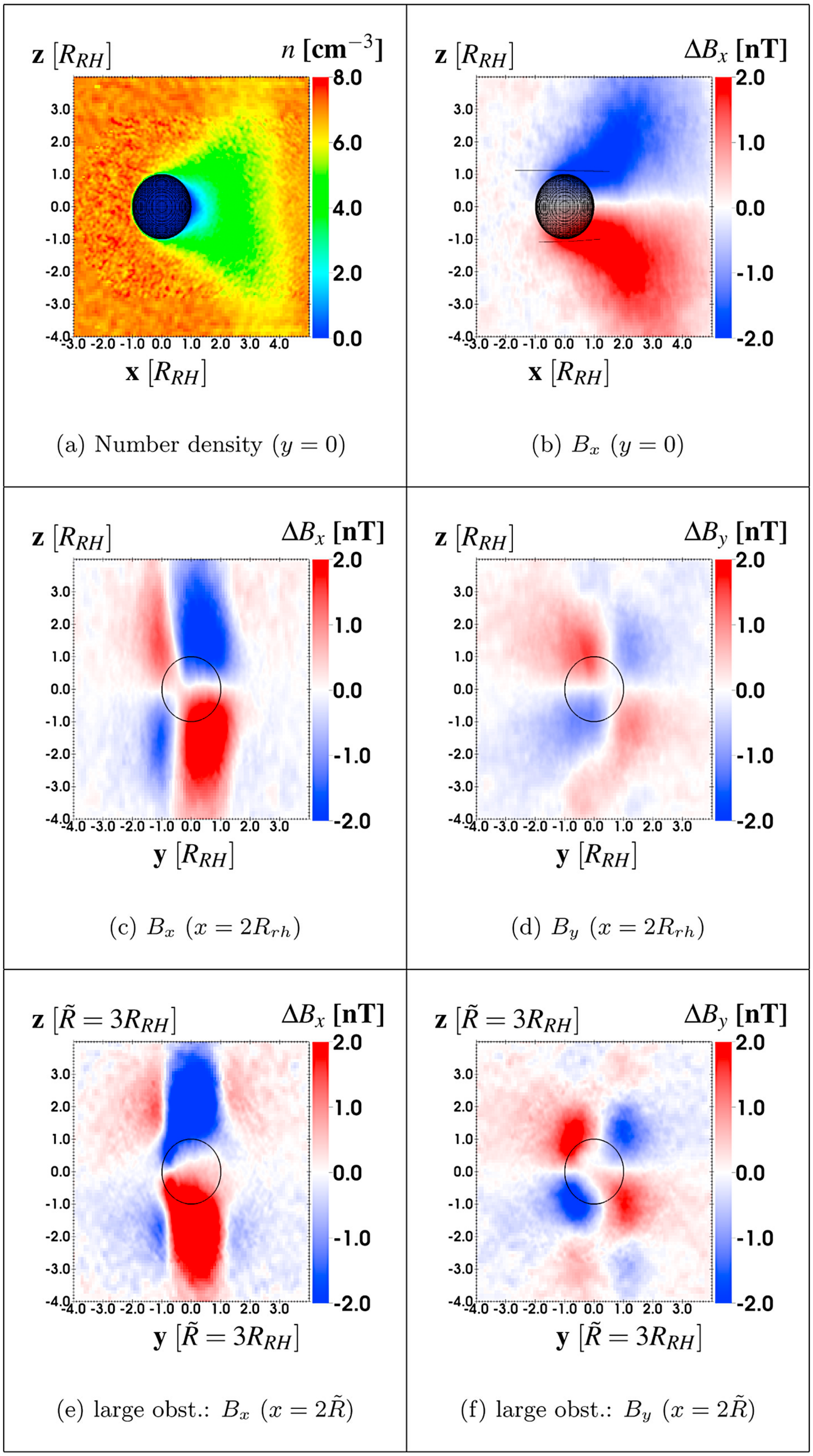
z [R_{RH}]
n [cm^{-3}]
x [R_{RH}]
(a) Number density ($y = 0$)
ΔB_x [nT]
(b) B_x ($y = 0$)
y [R_{RH}]
(c) B_x ($x = 2R_{rh}$)
ΔB_y [nT]
(d) B_y ($x = 2R_{rh}$)
z [$\tilde{R} = 3R_{RH}$]
y [$\tilde{R} = 3R_{RH}$]
(e) large obst.: B_x ($x = 2\tilde{R}$)
(f) large obst.: B_y ($x = 2\tilde{R}$)

Figure 4

the central wake and depressing the field at the flanks of the interaction region. They are also responsible for generating the quadrupolar pattern of different B_y orientations illustrated in Figure 1 of *Simon et al.* [2009]. The diamagnetic currents in x direction are closed within a current loop around the ramside of the satellite [see *Mauk et al.*, 2009, Figure 11.8].

3.3. Flyby R3: Hybrid Simulations

[45] So far, our analysis of the R3 magnetic field observations is mainly based on analytical estimates of the effects generating the perturbation signatures. In this way, we have been able to explain numerous features seen in the data set. However, to confirm that our interpretation is quantitatively realistic and to gain further insights into the current systems arising from the finite length of the wake –especially how j_{dia} is closed–, the interaction needs to be treated within the framework of a fully self-consistent plasma simulation. In addition, there is one feature in the R3 data set which has not yet been addressed: coincident with Cassini's outbound passage ($y < 0$) through the surface of the Rhea flux tube, the magnetometer detected a sharply pronounced dip in the B_x component with a magnitude of $\delta B_x \approx -2.1$ nT, i.e. comparable to the strength of the B_x enhancement seen within the Rhea flux tube.

[46] To clarify these remaining issues, we have applied the hybrid (kinetic ions, fluid electrons) simulation code AIKEF [*Müller et al.*, 2011] to carry out new simulations of Rhea's magnetospheric interaction, amplifying the pilot study by *Roussos et al.* [2008a]. Since the hybrid code treats the ions as individual particles, it is particularly suitable for reproducing effects associated with finite ion gyroradii, especially asymmetries in the flow deflection pattern and non-Maxwellian particle distribution functions (e.g., the ring distributions associated with ion pick-up or the counterstream distribution in the wake of an inert moon [cf. *Simon et al.*, 2009]).

[47] Since the key features and basic equations of this code have been elaborated on in detail by *Kriegel et al.* [2009, 2011] and *Müller et al.* [2010], we shall provide only a brief discussion of how this simulation code is adapted to the Rhea scenario.

3.3.1. Model Description and Input Parameters

[48] The magnetospheric upstream conditions applied in the simulations are provided in section 2.1. For the simulation of R3, however, three slight adjustments have been included: first, the weak tilt of the background magnetic field with respect to the z axis (see Figure 2, top right) has been taken into account and we set $\underline{B}_0 = (1.8, 0.6, -20.8)$ nT, i.e. the magnitude is again $B_0 \approx 21$ nT. Second, the upstream plasma density observed during R3 was also slightly larger than the value of $n_0 = 6$ cm^{-3} derived by *Wilson et al.* [2010] for R1 and R1.5. Measurements of Cassini's Radio and Plasma Wave Science Instrument suggest a value of $n_0 = 7$ cm^{-3} (E. Roussos et al., submitted, 2012), which we adopt as input parameter for our model. Third, while data from the R1 flyby [*Wilson et al.*, 2010] suggest an ion temperature of about $kT_i = 200$ eV, we achieved better agreement between simulation and MAG data for R3 by applying a value of $kT_i = 100$ eV, as proposed by *Roussos et al.* [2008a]. At the time of this writing, no measurements of the ion temperature were available for the R3 encounter. For this reason, we have used the ion temperature as a free parameter (within the range of values provided by *Wilson et al.* [2010], *Khurana et al.* [2008] and *Roussos et al.* [2008a]) to achieve best possible agreement between simulation and magnetic field data.

[49] The applied value of kT_i yields an ion gyroradius of $r_g = 0.45\ R_{rh}$. The modified upstream conditions yield an only slightly increased Alfvénic Mach number of M_A = 0.95 and a magnetosonic Mach number of M_{MS} = 0.73. While these changes have negligible qualitative influence on the overall structures seen in the simulations, they may nonetheless strongly affect the magnitudes of the signatures. The minor hydrogen component identified in CAPS ion data from R1 and R1.5 by *Wilson et al.* [2010] is not included in our simulations.

[50] In our hybrid simulations, Rhea is treated as an electromagnetically inert and plasma-absorbing body, i.e. the tenuous atmosphere described by *Teolis et al.* [2010] is not included. As discussed in our preceding publications [*Roussos et al.*, 2008a; *Kriegel et al.*, 2009, 2011], the AIKEF code does not impose any artificial boundary conditions on the electromagnetic fields in the obstacle's interior, but it solves Maxwell's equations for an Ohmic conductor in the inner region and realizes a self-consistent coupling to the electromagnetic fields in the adjacent plasma flow. The Ohmic conductivity of Rhea's interior is set to $\sigma = 5 \cdot 10^{-7}$ S/m [see also *Kriegel et al.*, 2009]. This value is small enough to prevent any noticeable currents from flowing through the non-conducting icy crust of the moon. Thus, the boundary condition for an icy satellite $\underline{j} \cdot \underline{e}_r = 0$ [*Neubauer*, 1998] –where $\underline{j}$ denotes the current density and $\underline{e}_r$ is the local radial unit vector– is fulfilled at Rhea's surface in good approximation. The simulation applies a hierarchical Cartesian grid with three different refinement levels, achieving a peak resolution of 0.05 R_{rh} near the surface of the moon. The resolution in the other two levels is two/four times larger. The simulation domain is cubic, possessing an extension of $-5\ R_{rh} \leq x \leq +10\ R_{rh}$ and $-7.5\ R_{rh} \leq y, z \leq +7.5\ R_{rh}$.

Figure 4. Hybrid simulation of Rhea's magnetospheric interaction for the conditions of the R3 encounter. The figure displays (a) the magnetospheric plasma density in the ($y = 0$) plane, (b) the magnetic B_x component in the ($y = 0$) plane, (c) the B_x component downstream of Rhea at $x = 2\ R_{rh}$ and (d) B_y at $x = 2\ R_{rh}$. Figures 4e and 4f show the results of a test simulation where the radius of Rhea has been artificially increased by a factor of 3 to investigate the influence of finite ion gyroradii on the interaction. In these two panels, the symbol $\tilde{R}$ refers to 3 × 764 km. The (e) B_x and (f) B_y components in the ($x = 2\ \tilde{R}$) plane are shown. In Figures 4b–4f, only the *perturbations* of the magnetic field are shown, i.e. the background magnetic field $\underline{B}_0$ has been subtracted. The cutting planes shown in Figures 4c, 4d, 4e and 4f are intersected by Rhea's geometric shadow $\sqrt{y^2 + z^2} = R_{rh}$ along the black circles. The outer, circle-like boundary visible in Figures 4e and 4f arises from different resolution levels of the simulation grid on either side.

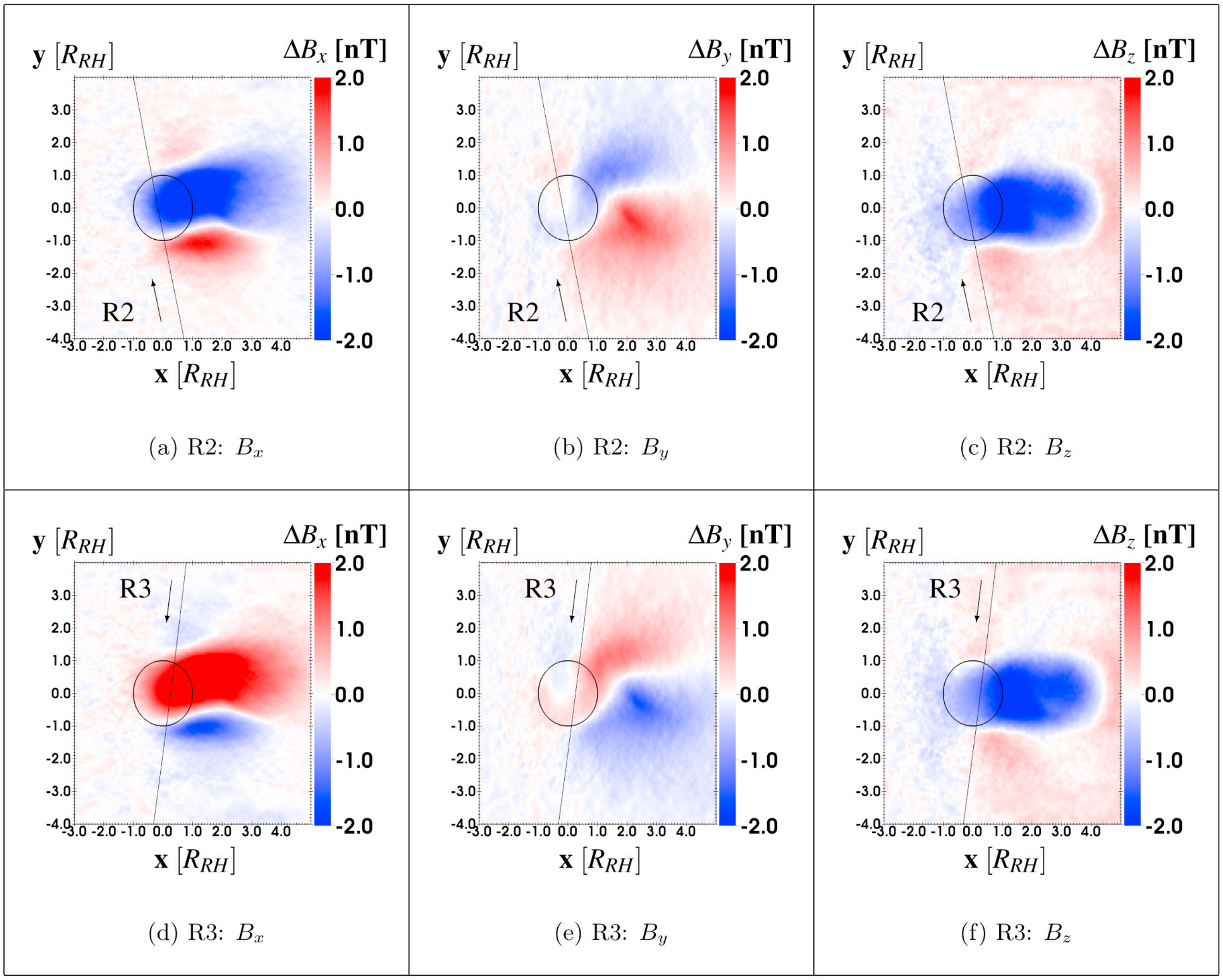

Figure 5. Perturbation magnetic field components (background field $\underline{B}_0$ subtracted) in the planes of the (a, b, c) R2 ($z = +1.1\ R_{rh}$) and (d, e, f) R3 ($z = -1.1\ R_{rh}$) flybys. The flyby trajectory is denoted by the black line, while the black circle $\sqrt{x^2 + y^2} = R_{rh}$ marks the projection of Rhea on the cutting planes.

3.3.2. Discussion of Simulation Results

[51] The results of our hybrid simulations can be seen in Figures 4, 5 and 6, respectively. Figures 4a and 4b display the magnetospheric plasma density and the corresponding B_x perturbation in the ($z = 0$) plane of the RHIS. For a downstream cut through the wake at $x = 2\ R_{rh}$, Figures 4c and 4d show the distortions of the B_x and B_y components.

[52] To explore the influence of the large ion gyroradii on the signatures seen in Figures 4c and 4d, Figures 4e and 4f display results from a test simulation where the radius of Rhea has been artificially increased by a factor of 3, while the incident flow parameters were left unchanged. Thus, the ion gyroradius is now $r_g = 0.15\ \tilde{R}$, where $\tilde{R}$ is the radius of the artificially enlarged obstacle. The purpose of this test scenario is to isolate the influence of finite gyroradius effects (i.e., highly asymmetric plasma absorption) on the structure of the magnetic field perturbations: while in the real Rhea scenario (Figures 4c and 4d, large gyroradii), the absorption process and the associated magnetic field perturbations feature a prominent asymmetry between the Saturn-facing ($y > 0$) and the Saturn-averted ($y < 0$) hemisphere, these signatures are nearly symmetric in the case of small ion gyroradii (Figures 4e and 4f).

[53] Figures 5d–5f display the perturbation magnetic field components in the plane of the R3 encounter (i.e. at $z = -1.1\ R_{rh}$), while Figure 6 shows a comparison between our model results and MAG data from R3 along the flyby trajectory. For the run illustrated by the solid red, green and blue lines (the results of this run are also shown in Figures 4 and 5), the upstream particle population is represented by a drifting Maxwellian distribution, i.e. the temperature is assumed to be isotropic and has a value of $kT_i = 100$ eV.

[54] In addition, the dashed lines illustrate the results of a test scenario where an anisotropic ion temperature has been included ($kT_{i,\perp} = 150$ eV, $kT_{i,\parallel} = 50$ eV). The applied values of the temperature components are similar to those shown in Figures 5 and 6 of *Wilson et al.* [2010] for the conditions of the R1 and R1.5 encounters. However, the results of this simulation obviously overestimate the magnitude of the observed B_z perturbation (indicative of the "strength" of the

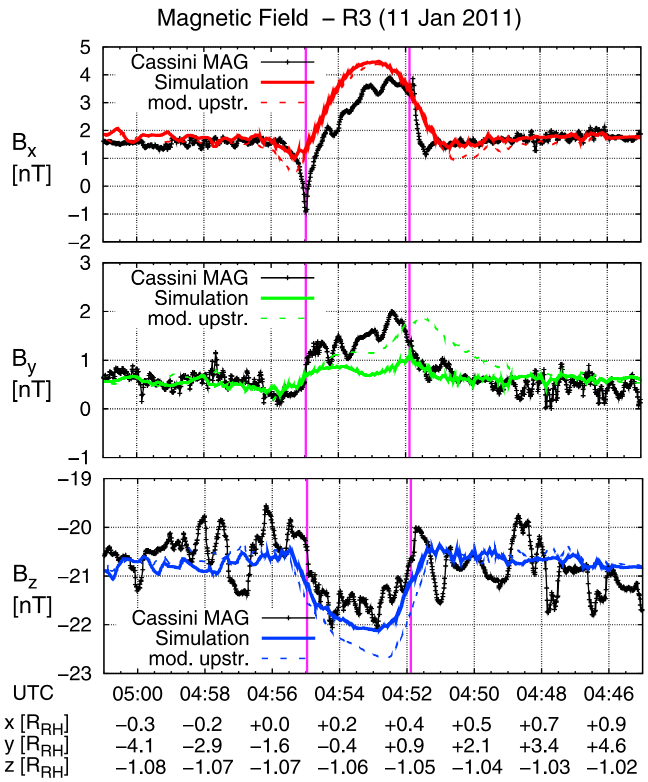

Figure 6. Cassini magnetic field observations (black) versus hybrid simulation results (B_x: red, B_y: green, B_z: blue) along the R3 trajectory. The solid lines show the results of the model run that yielded best agreement with MAG data. The dashed lines illustrate the results of a test scenario with an anisotropic temperature in the upstream flow. The vertical magenta lines denote Cassini's passages through the surface of the Rhea flux tube $\sqrt{x^2+y^2} = R_{rh}$. Similar to Figure 2, the data are shown from negative to positive y values (i.e. the time axis is reversed).

interaction) and are only meant to illustrate the general effect of an anisotropic temperature on the sharpness and depth of the simulated dip in the B_x component. Therefore, these results will only be briefly discussed at the end of the section. If not stated otherwise, the following discussion always refers to the case of an *isotropic* temperature, as illustrated by the *solid* red, green and blue lines in Figure 6.

[55] Figure 7 illustrates the number density of the magnetospheric plasma in the ($z = 0$) plane for both the real Rhea scenario (Figure 7a) and for the case of an artificially enlarged obstacle (Figure 7b). The influence of large ion gyroradii on the plasma absorption is also illustrated schematically in Figure 8.

[56] In accordance with preceding hybrid simulation results by *Roussos et al.* [2008a], Figure 4a illustrates that the region of depleted plasma density expands far north and south of Rhea along the magnetic field lines. With the initial conditions described by Mach numbers M_A = 0.95 and M_{MS} = 0.73, there are no real fast magnetosonic characteristics (see *Neubauer* [1998] for details), thereby implying continuous fast magnetosonic rarefaction flow everywhere, i.e. without fast mode discontinuities. Importantly a slow magnetosonic rarefaction wave is superimposed with a first order discontinuity at its front. This discontinuity connects tangentially to the Rhea surface and is characterized by an asymptotic slow mode Mach angle of 35°. The associated region of reduced density is visible in yellow and green in Figure 4a. Although not shown here again, the corresponding magnetic field enhancement in this region is similar to Figure 1(D) in the work of *Roussos et al.* [2008a]. The cone-like void region in Rhea's geometric shadow (denoted in blue) is clearly visible in the simulated density profile as well. We note that the expected discontinuous MHD structures are smeared out in the more accurate kinetic/hybrid description.

[57] In addition to the aforementioned structures, the simulation reveals two prominent regions of a reduced (for

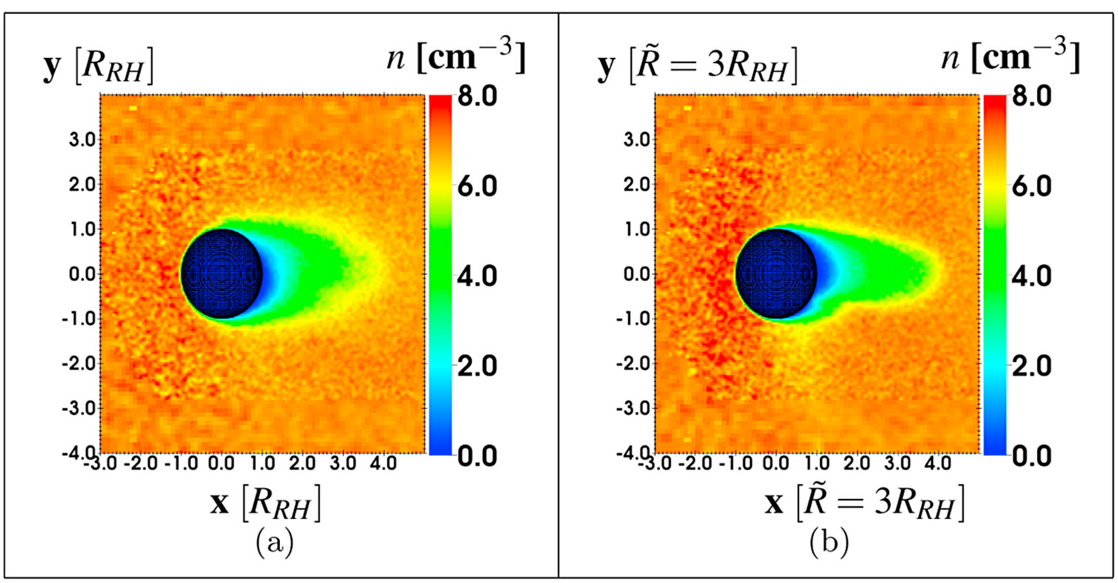

Figure 7. Number density of the magnetospheric plasma in the ($z = 0$) plane for the upstream conditions of the R3 flyby: (a) real Rhea scenario; (b) test scenario with artificially enlarged obstacle.

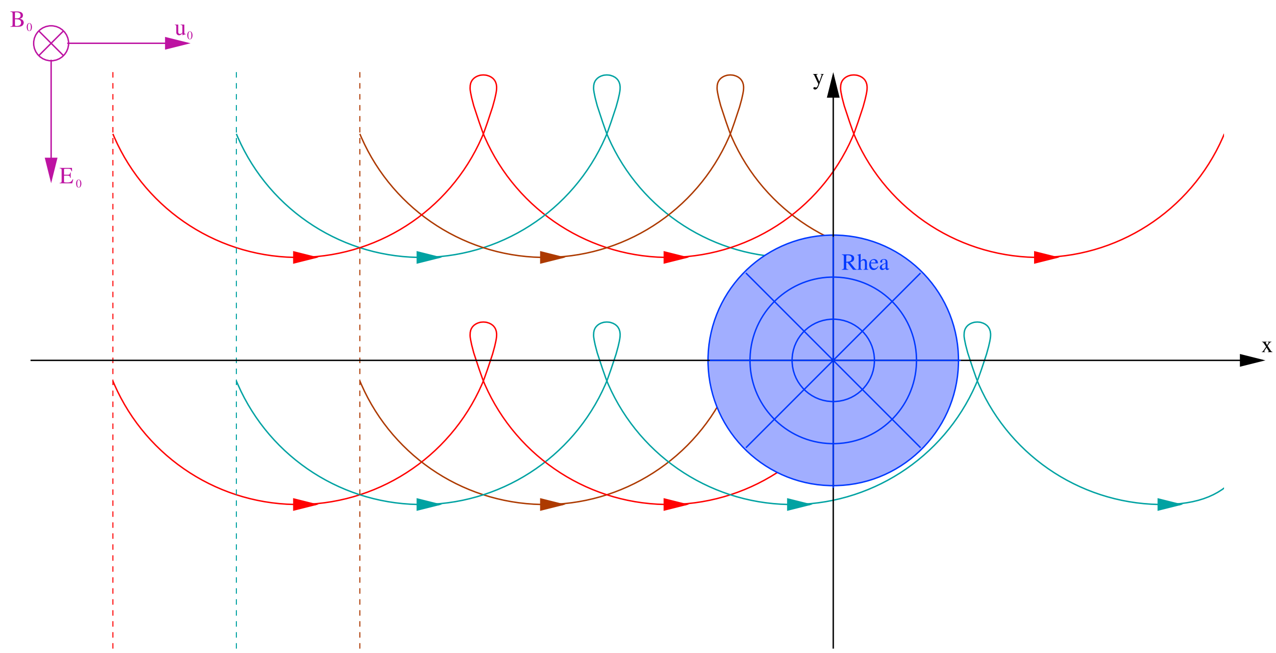

Figure 8. Asymmetric particle absorption at Rhea's surface. For the ($z = 0$) plane of the RHIS, the figure illustrates the trajectories of several representative magnetospheric ions in the vicinity of Rhea. In each $x =$ const plane upstream of the moon, the two red, cyan and brown particles possess the same gyrophase. However, in the ($y > 0$) half-space only the red particle "survives" the passage through the interaction region, while for $y < 0$ the cyan particle is the only one that does not get absorbed. Thus, the particle population reaching the downstream region in the Saturn-averted half-space possesses different gyrophases than the "surviving" particles in the Saturn-facing half-space. In the Saturn-averted half-space, particles which travel close to Rhea's surface (since the moon is located within a "bulge" of their trajectory) can reach the moon's wakeside, causing an asymmetry in the refilling of the density cavity. The cyan particle in the ($y < 0$) half-space possesses such a trajectory.

$z > 0$) or enhanced (for $z < 0$) B_x component, connecting to the near-Rhea region between the poles ($x = 0$) and $x \approx 4\ R_{rh}$, cf. Figure 4b. The sign of B_x corresponds to that of a magnetic draping pattern or an Alfvén wing, as it also arises from the interaction between the plume of Enceladus and the ambient magnetospheric flow [see, e.g., *Dougherty et al.*, 2006; *Simon et al.*, 2011b]. Indeed, the tilt angle of the simulated wings against the ambient magnetic field direction ($\approx \underline{e}_z$) corresponds well to a value of arctan $M_A \approx 44°$, as suggested by *Neubauer* [1980]. It should be noted that the Alfvénic field perturbation within these wings is rather weak, i.e. only about 10% of the magnetospheric background field.

[58] In order for an Alfvén wing to be formed, the currents along the wing characteristics need to be closed by transverse currents in the local interaction region. In the case of Enceladus, this closure is mediated by the Pedersen and Hall currents in the plume [*Saur et al.*, 2007; *Simon et al.*, 2011b]. At Rhea, however, we encounter a scenario where the current system of the wing is not closed within the obstacle's ionosphere, but by the diamagnetic current in ($-y$) direction that arises from the finite extension of the moon's wake along the corotational flow direction.

[59] The hybrid simulation revealed this Alfvénic interaction signature that was not considered in our original discussion of $\underline{j}_{dia}$. The formation of this Alfvén wing also implies that the diamagnetic currents in ($+y$) direction at the outer flanks of the wake are not strong enough to close the entire current system in ($-y$) direction, but the additional inclusion of the currents along the wing characteristics is required to fulfill the $\nabla \cdot \underline{j} = 0$ condition. In general, an Alfvén wing can form when the transverse currents $\underline{j}_\perp$ do not fulfill $\nabla \cdot \underline{j}_\perp = 0$, no matter whether the satellite possesses an atmosphere or not. It should be noted that in the scenario considered here, gradient and curvature drifts may also make a minor contribution to the perpendicular currents. Only for particles with energies in the keV range, these drift motions start to take major influence on particle dynamics, cf. Table 1 and section 7 in the work of *Khurana et al.* [2008].

[60] To further understand this peculiar structure, let us at first have a look at the simulated magnetic field configuration in a cut through the intermediate wake region at $x = 2\ R_{rh}$, see Figures 4c and 4d for the asymmetric case (large gyroradii) and Figures 4e and 4f where the gyroradii are small with respect to the artificially enlarged obstacle. In Figure 4e, one can recognize the magnetic field features typical for an Alfvén wing (see also *Neubauer* [1980] and Figure 8 in *Simon et al.* [2011b]). In planes perpendicular to the wing characteristics, the magnetic field configuration corresponds to a two-dimensional dipole whose magnetic moment has a component parallel (southern wing) or antiparallel (northern wing) to the positive x axis

of the RHIS. Correspondingly, a region of negative B_x is encountered within the center of the northern wing tube (dark blue region above Rhea in Figure 4e), while at the flanks of the northern wing tube, the field changes its orientation and points in positive x direction. In the southern hemisphere, the orientation of B_x is reversed inside and outside the wing. The quadrupolar pattern in the B_y component (see Figure 4f) corresponds to the field compression/plasma absorption pattern discussed in the preceding section.

[61] It is most important to note that if the gyroradii are small compared to the size of the obstacle, the magnitudes of the B_x and B_y perturbations are symmetric with respect to the ($x = 0$) plane, as illustrated by Figures 4e and 4f. In the real Rhea scenario, however, the large gyroradii of the magnetospheric upstream ions give rise to an asymmetrization of the B_x and B_y patterns with respect to the direction of the convective electric field $\underline{E}_0 \approx -u_0 B_0 \underline{e}_y$. As can be seen from Figure 4c, the draping pattern is clearly shifted in the ($y < 0$) half-space where the electric field points away from Rhea. The regions of perturbed B_x outside the Rhea flux tube become more prominent in the ($y < 0$) half-space, whereas for $y > 0$, both the magnitude and the extent of the B_x perturbations are reduced. In a similar way, the absorption pattern in the B_y component exhibits a slight asymmetry with respect to the direction of the convective electric field as well (see Figure 4d).

[62] A similar asymmetrization of the magnetic draping pattern with respect to the direction of the convective electric field occurs at Titan, where the gyroradii of both magnetospheric upstream ions and exospheric pick-up ions exceed the radius of the obstacle to the flow. By applying a hybrid simulation, *Simon et al.* [2007, 2008] showed that in this case, both the ramside magnetic pile-up region and the wakeside magnetotail structure are shifted in the direction of the convective electric field. These authors also found evidence for the asymmetric structure of Titan's interaction region in Cassini magnetic field observations.

[63] As can be seen from Figure 4c, the two wings near Rhea are not aligned with the direction of the background magnetic field, but they are both tilted away from Saturn. Since in the far field, an Alfvén wing exhibits translation symmetry along its characteristics $\underline{u}_0 \pm \underline{v}_A$ [*Neubauer*, 1980], this feature clearly illustrates that the B_x perturbations shown in Figure 4c cannot be exclusively ascribed to the current systems in the wing. In the rather small region around Rhea investigated here the transverse currents in the local interaction region make a noteworthy contribution that needs to be superimposed.

[64] While the asymmetries of Rhea's plasma interaction are clearly visible in the magnetic field (after subtraction of $\underline{B}_0$), they appear less prominent in the simulated plasma density near the moon. Overall, Figure 7 shows that in the real Rhea scenario, the wake is refilled at shorter distances to the moon than in the test scenario. This is best visible in the extension of the green density depletion region along the corotational flow direction. An explanation for this behavior is provided in Figure 8, showing that in the case of large gyroradii, the ions can refill the wake more easily by avoiding collisions with the moon on their spiral trajectories. Even in the case of small gyroradii, the density depletion region features a slight asymmetry. The occurrence of this effect is consistent with our preceding simulations of Tethys' magnetospheric interaction and arises from the Hall term [*Simon et al.*, 2009]. In the real Rhea scenario, this effect is still present (visible in the outer boundary of the green region in Figure 7a), although the outer flanks of the wake are more blurred. However, comparing the locations of the central density void downstream of the moon (dark blue region) between the real Rhea scenario (cf. Figure 7a) and the case of an artificially enlarged obstacle (cf. Figure 7b) also shows that in the real scenario, the central density void is more prominent in the Saturn-averted half-space where the convective electric field points away from Rhea. This effect may give rise to a slightly steeper density profile (along the corotation direction) for $y < 0$ than in the test scenario, generating a stronger diamagnetic current in the Saturn-averted half-space and thereby contributing to the asymmetry in the magnetic field pattern. Given the weakness of these visible modifications in the density profile (compared to the background density), it is also important to notice that the change in the magnitude of the B_x perturbation in the ($y < 0$) half-space between asymmetric and symmetric case (Figure 4c versus 4e) is on the order of only 1 nT, i.e. less than 5% of the background field.

[65] Based on these results, we can now investigate the origin of the spikey dip in B_x detected by Cassini when leaving the Rhea flux tube ($y < 0$). As can be seen from Figure 5d, Cassini only grazed the weakly pronounced region of reduced B_x in the inbound region of R3 ($y > 0$). However, after leaving the Rhea flux tube where B_x was enhanced, the spacecraft passed through the more prominent region of reduced B_x in the ($y < 0$) half-space. A comparison between measured and simulated B_x component (see Figure 6, top) shows that our simulation result is in good agreement with the measured B_x signature. Especially, both the magnitude and the width of the B_x enhancement inside the Rhea flux tube are quantitatively reproduced by the simulation. The location of the B_x dip at the ($y < 0$) surface of the Rhea flux tube is reproduced by the simulation as well, but its magnitude and sharpness are underestimated. A possible reason for this may be the finite level of numerical diffusion in the simulations or the occurrence of effects on electron scales which are not covered by the hybrid model. However, it is important to notice that our model qualitatively reproduces this dip by considering plasma-absorption at the moon's surface alone.

[66] To further illustrate that the effect producing the B_x spike seems to be reproduced by the hybrid simulation, let us have a brief look at the results of the test scenario with an *anisotropic* temperature (dashed red, green and blue lines in Figure 6). This run overestimates the width of the enhancement in B_y and especially the compression signature in B_z. Due to the increased perpendicular temperature (150 eV versus 100 eV), the pressure loss at Rhea's surface is larger than in the first simulation run, therefore requiring a stronger magnetic field enhancement.

[67] However, this run also produces a more prominent spike at the ($y < 0$) flank of the Rhea flux tube. These results illustrate that although the global features of the interaction remain qualitatively unaffected by the modified temperature, the magnitudes of the simulated magnetic field signatures

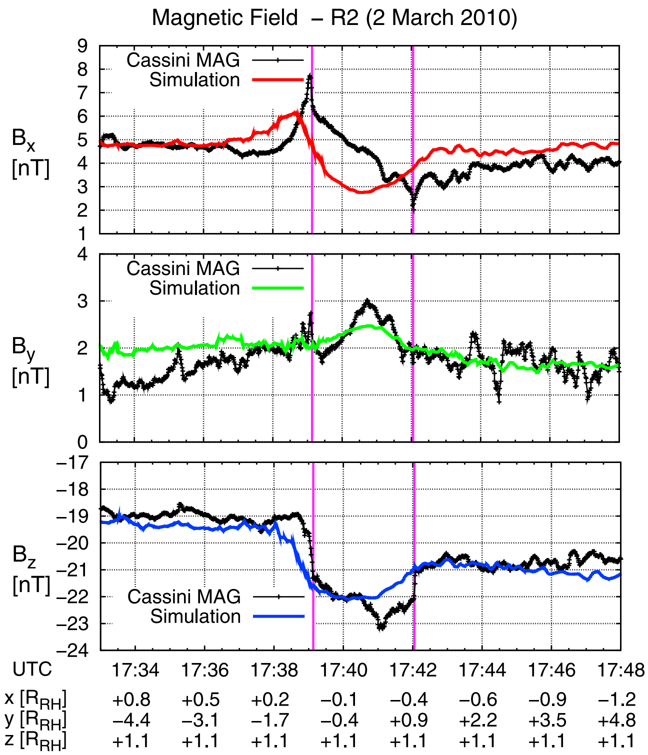

Figure 9. Cassini magnetic field observations (black) versus hybrid simulation results (B_x: red, B_y: green, B_z: blue) along the R2 trajectory. The vertical magenta lines denote Cassini's passages through the surface of the Rhea flux tube $\sqrt{x^2 + y^2} = R_{rh}$.

are highly sensitive to the incident magnetospheric flow conditions. To a high degree, the discrepancy between simulation and measurement near the ($y < 0$) passage through the Rhea flux tube may probably be ascribed to uncertainties in the ambient flow conditions. Of course, we cannot definitely exclude that additional effects which are not taken into account by the model –such as currents due to non-zero surface potentials [*Roussos et al.*, 2010; *Santolík et al.*, 2011]– might also play a role in causing the spikey shape of the observed signature. We would also like to point out that –based on the available data and modeling results– the question of why these spikes coincide almost precisely with Cassini's passage through the surface of the Rhea flux tube cannot be answered.

[68] As can be seen from Figure 6, the simulation also reasonably reproduces the positions and magnitudes of the perturbations seen in B_y and B_z. The contour plots in Figures 5d–5f place these spacecraft observations within the context of the three-dimensional interaction scenario. As discussed in section 3.2, the spacecraft only passed through the region of enhanced B_y during its south polar flyby. The simulation illustrates that this is not only a result of the inclination of the R3 trajectory against the y axis, but due to the large ion gyroradii, the B_y perturbations also exhibit a slight asymmetry between the ($y > 0$) and the ($y < 0$) half-spaces. Figure 5c illustrates that the maximum perturbation in B_z is indeed not achieved below the south pole where R3 took place, but further downstream in the central void region.

3.4. Flyby R2: MAG Observations and Hybrid Simulations

[69] In this section, we shall focus on Cassini's magnetic field observations during the north polar R2 encounter, as shown in Figure 2 (left). At first glance, the B_y and B_z perturbations are familiar to what is expected for the plasma interaction of an electromagnetically inert moon. Again, the magnetic field along the trajectory is compressed (i.e. $|B_z|$ is enhanced) within the Rhea flux tube, this time due to the depletion of magnetospheric particles incident upon Rhea's south pole. Even far outside the Rhea flux tube, the observed B_y component was highly perturbed. Although a slight enhancement of about 1 nT was detected within the Rhea flux tube, the magnitude of this perturbation is comparable to the B_y perturbations observed e.g., at $y = -5\ R_{rh}$ or at $y = +7\ R_{rh}$. The slight enhancement of B_y observed within the Rhea flux tube possibly arises from plasma absorption at Rhea's surface. The presence of a corresponding region of negative B_y (see upper sectors in Figure 1(ii) of *Simon et al.* [2009]) might have been obscured by the rather high fluctuation level that was present in the B_y component at the time of R2 (cf. Figure 2).

[70] At first glance, the B_x signature observed during R2 looks unusual. As can be seen from Figure 2, the magnetometer detected a bipolar perturbation in this component, with the positions of the maximum and the minimum coinciding with Cassini's passages through the surface of the Rhea flux tube. Considering that the spacecraft was moving mainly in y direction, the perturbation seen in B_x is similar to the magnetic field of a straight, infinitely long wire with the same diameter as the Rhea flux tube, carrying a homogeneous current in (+z) direction [see also *Santolík et al.*, 2011]. However, the occurrence of such an unidirectional current would be inconsistent with our interpretation of MAG data from the R3 flyby, involving a bipolar current system toward and away from Rhea in each of the two Alfvén wings. Note also that the variation in the observed B_x component outside the Rhea flux tube disagrees with the model of a cylindrical homogeneous current in z direction particularly before entering the flux tube [see *Santolík et al.*, 2011, Figure 3]. Also the model of a homogeneous wire predicts only weak variations in B_y, contrary to observations.

[71] To shed light on the origin of these puzzling B_x perturbations, we have carried out an additional hybrid simulation run for the R2 flyby. Again, the upstream flow conditions in the model differ slightly from the "average" set of parameters provided in section 2.1. First, the background magnetospheric field has been set to $\underline{B}_0 = (4.5, 1.7, -0.2y/R_{rh} - 20)$nT, accounting for the spatial inhomogeneity of the observed B_z component (see Figure 2, bottom left). The fundamental $\nabla \cdot \underline{B}_0 = 0$ condition is of course fulfilled by this setting. Second, the number density of the incident flow has been set to $n_0 = 4$ cm^{-3}, in agreement with Cassini observations (E. Roussos et al., submitted, 2012). However, these modifications of the upstream flow conditions again do not change the overall picture of the interaction, but only have quantitative impact on the magnitudes of the simulated field perturbations.

[72] As can be seen from Figure 9, both the width and the magnitude of the compression signature in B_z are well reproduced by the hybrid simulation. The model magnetic

field also shows a slight enhancement of B_y within the Rhea flux tube, in agreement with our expectations and Cassini MAG data. The simulated B_x signature exhibits a bipolar perturbation which is at least in rough qualitative agreement with Cassini observations. Although the magnitude of the peak field perturbation is quantitatively consistent with the observations as well, the sharpness of the two spikes is clearly underestimated by the model. Especially within the Rhea flux tube, the simulated B_x component decreases much steeper than the observed one. Overall, the simulated bipolar B_x perturbation is shifted against the measured one in negative y direction, with the displacement of the minimum being stronger than that of the maximum.

[73] A possible reason for this discrepancy may stem from non-stationarities in the incident magnetospheric flow conditions, as clearly visible in the B_y component. Additionally, Cassini Plasma Spectrometer data from preceding (close and non-targeted) Rhea encounters indicate that the ambient magnetospheric flow direction may possess a slight asymmetry between the Saturn-facing and the Saturn-averted half-space. *Wilson et al.* [2010] showed that during both, R1 and the non-targeted R1.5 encounter, the ambient flow possessed a radial component of about 10 km/s outward on the Saturn-averted side of Rhea, while no radial component was observed in the Saturn-facing hemisphere. Such asymmetric upstream flow conditions, which certainly impose additional deformations on the magnetic field lines in the interaction region, are not included in our hybrid simulation. Whether the varying radial flow profile derived by *Wilson et al.* [2010] is a result of Rhea's interaction with the magnetospheric flow or indeed a feature already present in the undisturbed upstream plasma is not yet clarified.

[74] However, it is also possible that there is still an important component missing in our understanding of Rhea's magnetospheric interaction during R2. Numerous unexplained features in particle data from R2 –such as the detection of dropouts in energetic particle fluxes outside the wake and the lack of a void region in the electron density downstream of Rhea– are in favor of this hypothesis (E. Roussos et al., submitted, 2012).

[75] Nevertheless, it is remarkable to notice that –in analogy to R3– by considering the plasma-absorbing body of Rhea alone, the hybrid model is able to qualitatively reproduce the bipolar nature of the observed B_x signature.

[76] The two-dimensional contour plots of the simulated magnetic field components in the plane of the R2 flyby (cf. Figures 5a–5c) illustrate the origin of the simulated B_x perturbation. Again, the spacecraft passed through the Alfvénic perturbation region that arises from the finite length of Rhea's wake. In the northern hemisphere where R2 took place, the B_x perturbation within the Rhea flux tube is negative, while B_x reverses its sign along the Saturn-facing and Saturn-averted flanks of the interaction region (see Figure 5a). Again, the large gyroradii of the incident ions make the perturbation features appear more prominent in the ($y < 0$) half-space.

[77] In analogy to R3, the combined influence of the slight tilt in the R2 flyby trajectory and the asymmetry of the field perturbation gave rise to the bipolar nature of the observed B_x signatures. When approaching Rhea from the Saturn-averted half-space, Cassini first intersected the region of positive B_x. Subsequently, the spacecraft penetrated the "core" of the Alfvénic flux tube, where the B_x perturbation possesses a negative sign. In the Saturn-facing half-space, the spacecraft missed the region of enhanced B_x at the flank of the interaction region for two reasons: on the one hand, the spacecraft moved into the undisturbed upstream hemisphere after closest approach to Rhea. On the other hand, the asymmetry of the Alfvénic perturbations between Saturn-facing and Saturn-averted hemisphere makes the B_x perturbation nearly vanish in the outbound region ($y > 0$) of the R2 flyby. In this sense, we propose that the B_x perturbations observed during R2 arise at least partially from the same mechanism as suggested for R3.

[78] It should be noted that only if a Rhea flyby occurred outside of the ($z = 0$) plane and downstream of about $x = 1$ R_{rh}, the spacecraft could potentially intersect the region of positive/negative B_x perturbation inside the southern/northern Alfvénic flux tube as well as *both* regions of negative/positive B_x perturbation along its flanks. However, neither the trajectories of R2 and R3 nor the preceding R1 flyby (at $z = 0$) meet this criterion. During the upcoming R4 encounter, Cassini will travel mainly in z direction along Rhea's Saturn-averted side with a closest approach altitude of 1.3 R_{rh}, thereby making it most likely impossible to collect further evidence for our interpretation. Available and scheduled flybys of Saturn's icy moons Tethys and Dione do not possess suitable trajectories for the detection of this effect either. In addition, the magnetic field arising from the diamagnetic currents may be much weaker at these moons. However, the idea of a weak, asymmetric Alfvén wing –arising from the finite length of Rhea's wake and the large gyroradii of the incident magnetospheric ions– can consistently explain Cassini MAG observations from the R2 and R3 flybys. Probably, these two encounters constitute the only icy satellite flybys of the entire Cassini mission whose trajectories were suitable to detect these peculiar features of an inert moon's plasma interaction.

[79] Finally, we would briefly like to dwell on an intrinsic limitation of the hybrid approach: while this type of model self-consistently encompasses non-Maxwellian ion distribution functions and the wave modes associated with their decay, it is not able to cover similar effects for the electrons. The decay of non-Maxwellian electron distributions (e.g. loss cones) may give rise to local inhomogeneities of the plasma temperature, affecting both the flow pattern and the magnetic field. Assessing the influence of these effects on Rhea's magnetospheric interaction would require the application of a full-particle model [*Birch and Chapman*, 2001], which –due to limited computing resources– is so far not available in three spatial dimensions. However, since we succeeded in explaining the key features of the magnetic field observations without inclusion of a self-consistent description of the electrons, we are confident that these effects will exert only weak influence on the structure of the interaction region. This assessment is further supported by magnetic field observations from the more distant R1 flyby, which could also be fully reproduced by a hybrid simulation that applies a simple adiabatic law to the electrons [*Roussos et al.*, 2008a].

[80] In their study of Tethys' magnetospheric interaction, *Simon et al.* [2009] explored the impact of changes in the (spatially homogeneous) electron temperature on the plasma flow and magnetic field pattern in the wake. These authors

showed that even an increase of the electron temperature by a factor of 4 had only minor quantitative influence on the magnetic field signatures and the density pattern (see especially Figure 3 in that work). Hence, it is reasonable to expect that spatial inhomogeneities of the electron temperature will not introduce additional new features in the large-scale magnetic field environment of Saturn's plasma-absorbing moons.

4. Summary and Concluding Remarks

[81] In this study, we have presented an analysis of Cassini magnetic field data acquired during the only two polar Rhea flybys of the entire Cassini mission. During the R2 flyby on 02 March 2010, Cassini passed through the Rhea flux tube $\sqrt{y^2 + z^2} = R_{rh}$ above the north pole while moving from the Saturn-averted into the Saturn-facing half-space. The trajectory of the subsequent R3 encounter on 11 January 2011 led through the Rhea flux tube below the moon's south pole. During R3, Cassini moved from the Saturn-facing into the Saturn-averted half-space. The trajectories of both flybys were nearly parallel to Rhea's equatorial plane ($z = 0$) and slightly inclined with respect to the y axis. During the entire Cassini mission, there will be no further Rhea flybys that possess similar trajectories. Magnetic field observations from both flybys revealed perturbation signatures inside the Rhea flux tube with a magnitude of about 10–15% of the background field.

[82] To interpret these magnetic field observations, we have applied estimations from simple analytical models as well as output from a hybrid plasma simulation (kinetic ions, fluid electrons). Our major results can be summarized as follows:

[83] Even though data from Cassini's Ion and Neutral Mass Spectrometer suggest Rhea to be embedded in a tenuous exosphere [*Teolis et al.*, 2010], the interaction between this gas envelope and the incident magnetospheric flow is not expected to produce any measurable perturbations of the ambient magnetic field. Since the Pedersen conductance of Rhea's exosphere is about two orders of magnitude smaller than the Alfvén conductance of the ambient flow, the weak Alfvén wing arising from the presence of the atmosphere is completely obscured by the magnetic field signatures caused by plasma absorption at the surface.

[84] Although Cassini did not pass through the wake downstream of Rhea, the magnetometer detected compression signatures in B_z during both flybys. These field perturbations arise from the absorption of magnetospheric particles with large field-aligned velocity components at the surface of the icy moon: particle absorption in the south polar region leads to a partial depletion of the magnetospheric flow above the north pole. On the other hand, absorption of particles impinging with pitch angles near 0° (remember that $\underline{B}_0$ points southward) on the north pole causes a plasma void below the south pole. The resulting pressure deficit within the Rhea flux tube is compensated by an enhanced magnetic field strength. The magnitude of the observed B_z perturbations is consistent with a simple pressure balance calculation. The signatures seen in B_y during both flybys are also consistent with a compression of the magnetic field lines inside the Rhea flux tube and a depression along the flanks of the interaction region. This picture agrees well with Cassini MAG observations during flybys of Dione and Tethys as well as during an earlier wakeside Rhea encounter [e.g., *Roussos et al.*, 2008a; *Simon et al.*, 2009, 2011a].

[85] Due to the high thermal velocity of the incident magnetospheric flow, the density void downstream and over the poles of Rhea is refilled at rather short distances of 2–3 moon radii along the corotational flow direction. The resulting density gradient in ($+x$) direction gives rise to a diamagnetic current in ($-y$) direction, i.e. parallel to the undisturbed convective electric field. This diamagnetic current is connected to the currents along the characteristics of a weak Alfvén wing, arising from the finite length of Rhea's plasma wake in ($+x$) direction. The presence of this wing corresponds to a negative B_x perturbation above the north pole and to a positive B_x perturbation below the south pole of Rhea. Thus, the finite length of Rhea's plasma wake produces a qualitatively similar perturbation as field line draping around a conducting exosphere/ionosphere. A minor part of the diamagnetic currents is closed at the outer boundaries of Rhea's plasma wake. In these regions, the density gradient points in negative x direction, corresponding to a diamagnetic current in positive y direction.

[86] The intensity of the flow-aligned magnetic field perturbations is not only proportional to the pressure gradient in the wake, but it also *decreases* with *increasing* strength of the ambient magnetospheric field. The plasma environment of Rhea, featuring a rather large beta value of $\beta_i + \beta_e \approx 1$, is therefore particularly suitable for observing these signatures. Even if flybys of Tethys or Dione possessed suitable trajectories to detect this effect, the stronger background magnetospheric field near the orbits of these satellites ($\beta_i + \beta_e \ll 1$) would most probably prevent the formation of any measurable flow-aligned field perturbations.

[87] At Rhea, the ion gyroradii in the incident magnetospheric flow are comparable to the size of the obstacle, thereby making plasma absorption at the surface of the moon asymmetric with respect to the direction of the convective electric field. This effect also causes an asymmetry in the structure of the Alfvén wing: in the Saturn-averted hemisphere where the convective electric field points away from Rhea, the magnetic field perturbations are more intense than in the Saturn-facing hemisphere. Magnetic field observations from both R2 and R3 are qualitatively consistent with the presence of this asymmetric Alfvén wing structure, generated by the finite length of Rhea's wake. Additional close flybys of Rhea are required to further strengthen this prediction of our hybrid simulation model. However, at least during the Cassini mission, no additional Rhea flybys with a suitable trajectory will take place.

[88] Regarding the exploration of Saturn's icy satellites (except for Enceladus), the Cassini mission has already passed its summit. Only one additional targeted flyby of Rhea (R4) is scheduled for 09 March 2013. Two additional close flybys of Dione (D4 on 16 June 2015 and D5 on 17 August 2015) then finally denote the end of Cassini's visits to Saturn's family of inactive icy moons. However, the findings of this study (among others) clearly demonstrate that our understanding of the interaction between Saturn's icy satellites and their magnetospheric environment is far from complete. The scientific community could strongly benefit from the inclusion of additional visits to these fascinating solar system objects in the Cassini tour.

[89] **Acknowledgments.** S. Simon and H. Kriegel contributed equally to this work. The authors are grateful to both referees for careful inspection of the manuscript and for valuable comments. S^2 and H.K. acknowledge helpful discussions with Joachim Mueller and Yoann Vernisse (TU Braunschweig). The work of H.K. and U.M. was financially supported by the Deutsche Forschungsgemeinschaft (DFG) under grant MO539/19-1. The work of S^2 and J.S. was partially supported by the DFG under grant SI1753/1-1. The hybrid simulations were performed on the JUROPA supercomputers at the Juelich Supercomputing Centre, Forschungszentrum Juelich (Germany).

[90] Masaki Fujimoto thanks the reviewers for their assistance in evaluating this paper.

References

Birch, P. C., and S. C. Chapman (2001), Particle-in-cell simulations of the lunar wake with high phase space resolution, *Geophys. Res. Lett.*, *28*, 219–222, doi:10.1029/2000GL011958.

Burch, J. L., J. Goldstein, W. S. Lewis, D. T. Young, A. J. Coates, M. K. Dougherty, and N. André (2007), Tethys and Dione as sources of outward-flowing plasma in Saturn's magnetosphere, *Nature*, *447*(7146), 833–835, doi:10.1038/nature05906.

Colburn, D. S., R. G. Currie, J. D. Mihalov, and C. P. Sonett (1967), Diamagnetic solar-wind cavity discovered behind moon, *Science*, *158*(3804), 1040–1042, doi:10.1126/science.158.3804.1040.

Dougherty, M. K., et al. (2004), The Cassini magnetic field investigation, *Space Sci. Rev.*, *114*, 331–383, doi:10.1007/s11214-004-1432-2.

Dougherty, M. K., et al. (2005), Cassini magnetometer observations during Saturn orbit insertion, *Science*, *307*(5713), 1266–1270, doi:10.1126/science.1106098.

Dougherty, M. K., K. K. Khurana, F. M. Neubauer, C. T. Russell, J. Saur, J. S. Leisner, and M. E. Burton (2006), Identification of a dynamic atmosphere at Enceladus with the Cassini magnetometer, *Science*, *311*(5766), 1406–1409, doi:10.1126/science.1120985.

Jones, G. H., et al. (2008), The dust halo of Saturn's largest icy moon, Rhea, *Science*, *319*(5868), 1380–1384, doi:10.1126/science.1151524.

Kallio, E. (2005), Formation of the lunar wake in quasi-neutral hybrid model, *Geophys. Res. Lett.*, *32*, L06107, doi:10.1029/2004GL021989.

Khurana, K. K., C. T. Russell, and M. K. Dougherty (2008), Magnetic portraits of Tethys and Rhea, *Icarus*, *193*, 465–474, doi:10.1016/j.icarus.2007.08.005.

Kriegel, H., S. Simon, J. Müller, U. Motschmann, J. Saur, K. Glassmeier, and M. K. Dougherty (2009), The plasma interaction of Enceladus: 3D hybrid simulations and comparison with Cassini MAG data, *Planet. Space Sci.*, *57*(14–15), 2113–2122, doi:10.1016/j.pss.2009.09.025.

Kriegel, H., S. Simon, U. Motschmann, J. Saur, F. M. Neubauer, A. M. Persoon, M. K. Dougherty, and D. A. Gurnett (2011), Influence of negatively charged plume grains on the structure of Enceladus' Alfvén wings: Hybrid simulations versus Cassini MAG data, *J. Geophys. Res.*, *116*, A10223, doi:10.1029/2011JA016842.

Mauk, B. H., et al. (2009), Fundamental Plasma Processes in Saturn's Magnetosphere, in *Saturn From Cassini-Huygens*, edited by M. K. Dougherty, L. W. Esposito, and S. M. Krimigis, pp. 281–331, Springer Netherlands, Heidelberg, Germany.

Müller, J., S. Simon, U. Motschmann, K. H. Glassmeier, J. Saur, J. Schuele, and G. J. Pringle (2010), Magnetic field fossilization and tail reconfiguration in Titan's plasma environment during a magnetopause passage: 3D adaptive hybrid code simulations, *Planet. Space Sci.*, *58*(12), 1526–1546, doi:10.1016/j.pss.2010.07.018.

Müller, J., S. Simon, U. Motschmann, J. Schüle, K. Glassmeier, and G. J. Pringle (2011), A.I.K.E.F.: Adaptive hybrid model for space plasma simulations, *Comput. Phys. Commun.*, *182*(4), 946–966, doi:10.1016/j.cpc.2010.12.033.

Neubauer, F. M. (1980), Nonlinear standing Alfven wave current system at Io: Theory, *J. Geophys. Res.*, *85*, 1171–1178, doi:10.1029/JA085iA03p01171.

Neubauer, F. M. (1998), The sub-Alfvénic interaction of the Galilean satellites with the Jovian magnetosphere, *J. Geophys. Res.*, *103*, 19,843–19,866, doi:10.1029/97JE03370.

Neubauer, F. M., D. A. Gurnett, J. D. Scudder, and R. E. Hartle (1984), Titan's magnetospheric interaction, in *Saturn*, edited by T. Gehrels and M. S. Matthews, pp. 760–787, Univ. of Ariz. Press, Tucson.

Roussos, E., J. Mueller, S. Simon, A. Boesswetter, U. Motschmann, N. Krupp, M. Fraenz, J. Woch, K. K. Khurana, and M. K. Dougherty (2008a), Plasma and fields in the wake of Rhea: 3-D hybrid simulation and comparison with Cassini data, *Ann. Geophys.*, *26*(3), 619–637.

Roussos, E., N. Krupp, T. P. Armstrong, C. Paranicas, D. G. Mitchell, S. M. Krimigis, G. H. Jones, K. Dialynas, N. Sergis, and D. C. Hamilton (2008b), Discovery of a transient radiation belt at Saturn, *Geophys. Res. Lett.*, *35*, L22106, doi:10.1029/2008GL035767.

Roussos, E., N. Krupp, H. Krüger, and G. H. Jones (2010), Surface charging of Saturn's plasma-absorbing moons, *J. Geophys. Res.*, *115*, A08225, doi:10.1029/2010JA015525.

Santolík, O., D. A. Gurnett, G. H. Jones, P. Schippers, F. J. Crary, J. S. Leisner, G. B. Hospodarsky, W. S. Kurth, C. T. Russell, and M. K. Dougherty (2011), Intense plasma wave emissions associated with Saturn's moon Rhea, *Geophys. Res. Lett.*, *38*, L19204, doi:10.1029/2011GL049219.

Saur, J., and D. F. Strobel (2005), Atmospheres and plasma interactions at Saturn's largest inner icy satellites, *Astrophys. J.*, *620*(2), L115–L118, doi:10.1086/428665.

Saur, J., F. M. Neubauer, D. F. Strobel, and M. E. Summers (1999), Three-dimensional plasma simulation of Io's interaction with the Io plasma torus: Asymmetric plasma flow, *J. Geophys. Res.*, *104*, 25,105–25,126, doi:10.1029/1999JA900304.

Saur, J., F. M. Neubauer, and N. Schilling (2007), Hemisphere coupling in Enceladus' asymmetric plasma interaction, *J. Geophys. Res.*, *112*, A11209, doi:10.1029/2007JA012479.

Saur, J., N. Schilling, F. M. Neubauer, D. F. Strobel, S. Simon, M. K. Dougherty, C. T. Russell, and R. T. Pappalardo (2008), Evidence for temporal variability of Enceladus' gas jets: Modeling of Cassini observations, *Geophys. Res. Lett.*, *35*, L20105, doi:10.1029/2008GL035811.

Sergis, N., et al. (2010), Particle pressure, inertial force, and ring current density profiles in the magnetosphere of Saturn, based on Cassini measurements, *Geophys. Res. Lett.*, *37*, L02102, doi:10.1029/2009GL041920.

Simon, S., A. Boesswetter, T. Bagdonat, U. Motschmann, and J. Schuele (2007), Three-dimensional multispecies hybrid simulation of Titan's highly variable plasma environment, *Ann. Geophys.*, *25*(1), 117–144.

Simon, S., U. Motschmann, G. Kleindienst, K.-H. Glassmeier, C. Bertucci, and M. K. Dougherty (2008), Titan's magnetic field signature during the Cassini T34 flyby: Comparison between hybrid simulations and MAG data, *Geophys. Res. Lett.*, *35*, L04107, doi:10.1029/2007GL033056.

Simon, S., J. Saur, F. Neubauer, U. Motschmann, and M. Dougherty (2009), Plasma wake of Tethys: Hybrid simulations versus Cassini MAG data, *Geophys. Res. Lett.*, *36*, L04108, doi:10.1029/2008GL036943.

Simon, S., J. Saur, F. M. Neubauer, A. Wennmacher, and M. K. Dougherty (2011a), Magnetic signatures of a tenuous atmosphere at Dione, *Geophys. Res. Lett.*, *38*, L15102, doi:10.1029/2011GL048454.

Simon, S., J. Saur, H. Kriegel, F. Neubauer, U. Motschmann, and M. Dougherty (2011b), Influence of negatively charged plume grains and hemisphere coupling currents on the structure of Enceladus' Alfvén wings: Analytical modelling of Cassini magnetometer observations, *J. Geophys. Res.*, *116*, A04221, doi:10.1029/2010JA016338.

Sittler, E. C., et al. (2006), Cassini observations of Saturn's inner plasmasphere: Saturn orbit insertion results, *Planet. Space Sci.*, *54*(12), 1197–1210, doi:10.1016/j.pss.2006.05.038.

Sittler, E. C., et al. (2007), Erratum to Cassini observations of Saturn's inner plasmasphere: Saturn orbit insertion results. [Planetary and Space Science 54 (2006) 1197 1210], *Planet. Space Sci.*, *55*(14), 2218–2220, doi:10.1016/j.pss.2006.11.022.

Teolis, B. D., et al. (2010), Cassini finds an oxygen-carbon dioxide atmosphere at Saturn's icy moon Rhea, *Science*, *330*(6012), 1813–1815, doi:10.1126/science.1198366.

Tiscareno, M. S., J. A. Burns, J. N. Cuzzi, and M. M. Hedman (2010), Cassini imaging search rules out rings around Rhea, *Geophys. Res. Lett.*, *37*, L14205, doi:10.1029/2010GL043663.

Tokar, R. L., R. E. Johnson, M. F. Thomsen, E. C. Sittler, A. J. Coates, R. J. Wilson, F. J. Crary, D. T. Young, and G. H. Jones (2012), Detection of exospheric O_2^+ at Saturn's moon Dione, *Geophys. Res. Lett.*, *39*, L03105, doi:10.1029/2011GL050452.

Wilson, R. J., R. L. Tokar, W. S. Kurth, and A. M. Persoon (2010), Properties of the thermal ion plasma near Rhea as measured by the Cassini plasma spectrometer, *J. Geophys. Res.*, *115*, A05201, doi:10.1029/2009JA014679.